

Characterising the orbit and circumstellar environment of the high-mass binary MWC 166 A

Sebastian A. Zarrilli¹, Stefan Kraus¹, Alexander Kreplin¹, John D. Monnier², Tyler Gardner², Antoine Mérand⁵, Sam Morrell¹, Claire L. Davies¹, Aaron Labdon^{1,5}, Jacob Ennis², Benjamin Setterholm², Jean-Baptiste Le Bouquin³, Narsireddy Anugu⁴, Cyprien Lanthermann⁴, Gail Schaefer⁴, and Theo ten Brummelaar⁴

(1) University of Exeter, School of Physics and Astronomy, Astrophysics Group, Stocker Road, Exeter, EX4 4QL, UK

(2) University of Michigan, Department of Astronomy, S University Avenue, Ann Arbor, MI 48109, USA

(3) Institut de Planetologie et d'Astronomie de Grenoble, Grenoble 38058, France

(4) The CHARA Array of Georgia State University, Mount Wilson Observatory, Mount Wilson, CA 91023, USA

(5) European Organisation for Astronomical Research in the Southern Hemisphere (ESO), Karl-Schwarzschild-Str. 2, 85748 Garching bei München, Germany

Received 27 May, 2022; accepted 30 June, 2022

ABSTRACT

Context. Stellar evolution models are highly dependent on accurate mass estimates, especially for highly massive stars in the early stages of stellar evolution. The most direct method for obtaining model-independent stellar masses is derivation from the orbit of close binaries.

Aims. Our aim was to derive the first astrometric+radial velocity orbit solution for the single-lined spectroscopic binary star MWC 166 A, based on near-infrared interferometry over multiple epochs and ~100 archival radial velocity measurements, and to derive fundamental stellar parameters from this orbit. A supplementary aim was to model the circumstellar activity in the system from *K*-band spectral lines.

Methods. The data used include interferometric observations from the VLTI instruments GRAVITY and PIONIER, as well as the MIRC-X instrument at the CHARA Array. We geometrically modelled the dust continuum to derive relative astrometry at 13 epochs, determine the orbital elements, and constrain individual stellar parameters at four different age estimates. We used the continuum models as a base to examine differential phases, visibilities and closure phases over the Br γ and He I emission lines, in order to characterise the nature of the circumstellar emission.

Results. Our orbit solution suggests a period of $P = 367.7 \pm 0.1$ d, approximately twice as long as found with previous radial velocity orbit fits. We derive a semi-major axis of 2.61 ± 0.04 au at $d = 990 \pm 50$ pc, an eccentricity of 0.498 ± 0.001 and an orbital inclination of $53.6 \pm 0.3^\circ$. This allowed constraint of the component masses to $M_1 = 12.2 \pm 2.2 M_\odot$ and $M_2 = 4.9 \pm 0.5 M_\odot$.

Conclusions. The line-emitting gas was found to be localised around the primary and is spatially resolved on scales of ~ 11 stellar radii, where the spatial displacement between the line wings is consistent with a rotating disc. The large spatial extent and stable rotation axes orientation measured for the Br γ and He I line emission are inconsistent with an origin in magnetospheric accretion or boundary-layer accretion, but indicate a ionised inner gas disk around this Herbig Be star. We observe line variability that could be explained either with generic line variability in a Herbig star disc or V/R variations in a decretion disc scenario. We have also constrained the age of the system, with relative flux ratios suggesting an age of $\sim (7 \pm 2) \times 10^5$ yr, consistent with the system being comprised of a main-sequence primary and a secondary still contracting towards the main-sequence stage.

Key words. Stars: fundamental parameters - Stars: individual: MWC 166 A – Stars: emission-line, Be – Techniques: interferometric

1. Introduction

The masses and ages of young stellar objects (YSOs) are commonly derived from comparison of observed positions on a colour-magnitude diagram to theoretical models (e.g. Siess et al. 2000; Baraffe et al. 2015; Choi et al. 2016). Evolutionary tracks of YSOs are very sensitive to mass, and as such need to be calibrated from observed systems with well-constrained masses. The relative paucity of higher-mass Herbig Ae/Be YSOs ($\gtrsim 5M_\odot$) compared to their lower-mass T Tauri counterparts means that models of higher-mass stars are less thoroughly calibrated. The high effective temperature of Herbig Be stars ($\gtrsim 15000$ K), as well as their often-uncertain ages due to mass loss from stellar winds, make it much less straightforward to calculate their

masses (Massey et al. 2012). Stassun et al. (2014) found that predicted and measured masses can differ by ~10%.

The gold standard for deriving model-independent masses is by taking advantage of the orbital mechanics of binary systems. If both astrometric and radial velocity (RV) data are used, the derived orbital parameters can be combined with reliable distance estimates (if any exist) to extract dynamical masses for the individual objects. This requires observation of a binary system at multiple epochs spread over a substantial fraction of the orbit, so targets with relatively short orbits and small separations are the best candidates. The need for precise astrometry on very small angular scales (~1 mas) has hugely benefitted from the relatively recent development of optical and near-infrared (NIR)

interferometry, which has ‘unlocked’ a larger tranche of suitable systems compared to even fifteen years ago.

A typical feature of YSOs is the presence of substantial amounts of circumstellar material left over from stellar formation, taking the form of a disc due to conservation of angular momentum. In single systems, dispersal of the disc occurs from a combination of accretion onto the star, depletion from stellar wind, and condensation into protoplanets, with a typical disc lifetime of 1-3 Myr (Li & Xiao 2016). However, the picture is more complicated when binary systems are concerned. If the binary is widely separated, each individual star can host its own circumstellar disc, but for many luminous and close Herbig Ae/Be binaries, a single circumbinary disc is the only possible structure for circumstellar material (Pichardo et al. 2005). This is due to dynamical interactions between the stars and the disc, which can affect both the accretion properties of the system and the disc’s shape and lifetime, although it is unclear under what conditions they will either delay or accelerate disc dispersal (Cieza et al. 2009). Dynamical truncation will affect the potential of the disc to form planetary systems by removing or rearranging the material available for planet formation. The known population of circumbinary planets has been substantially increased by Kepler observations (e.g. Doyle et al. 2011), and numerical simulations suggest that features rare in planets around single stars, such as large eccentricities and planet-star misalignment, are more common in circumbinary systems (Chen et al. 2019). Further studies on well-characterised young multiple star systems are also essential to study other dynamical mechanisms that might shape the architecture of exoplanetary systems, for instance by moving disc material onto oblique orbits (Kraus et al. 2020).

The focus of this study is the multiple system MWC 166 (= HD 53367, HIP 34116, V750 Mon). This is a hierarchical triple system, with a close spectroscopic binary (MWC 166 A) orbited by a wide companion (MWC 166 B) at a separation of 0.6'' (Fabricius et al. 2002). The radial velocity (RV) variations of the spectroscopic binary have first been reported by Finkenzeller & Mundt (1984) and tentative spectroscopic orbit solutions have been presented by Corporon & Lagrange (1999) and Pogodin et al. (2006). In this paper, we focus on this inner spectroscopic binary, the components of which have been labelled MWC 166 Aa and MWC 166 Ab throughout.

MWC 166 is located in the nearby OB association Canis Major OB1, whose age has been estimated to be ~ 3 Myr (Clariá 1974). The object also features significant mid-infrared to millimetre excess, which is indicative of a disc around MWC 166 A. The distance to the OB association has been estimated to 1150 ± 140 pc (Clariá 1974). Subsequent photometric measurements taken from a larger number of sources broadly agree with this value and have more tightly constrained it to 990 ± 50 pc (Shevchenko et al. 1999; Kaltcheva & Hilditch 2000).

Here, we present near-infrared interferometric observations obtained with the Very Large Telescope Interferometer (VLTI) and the Center for High-Angular Resolution Astronomy (CHARA; ten Brummelaar et al. 2005) Array, which have allowed us to derive a first astrometric orbital solution of the system. We present our observations in Sect. 2, followed by a discussion of our modelling approach (Sect. 3). We derive the orbit solution and dynamical mass constraints in Sect. 4, while spectral line analysis results are presented in Sect. 5. A discussion on the distribution of circumstellar material – both in the dust continuum and in prominent K -band emission lines – is presented in Sect. 6, and our conclusions are summarised in Sect. 7.

2. Observations

Near-infrared interferometric observations were taken over a period of 8 years, mainly using the PIONIER (Le Bouquin et al. 2011) and GRAVITY (Gravity Collaboration et al. 2017) 4-beam combiners at the VLTI. All VLTI observations employed the 1.8-metre Auxiliary Telescopes. Longer baselines were provided by 4-telescope observations using the CHARA Array instrument MIRC-X (Kraus et al. 2018; Anugu et al. 2020).

The GRAVITY observations were taken in the K -band (1.99–2.45 μm) as part of ESO programme 098.C-0910(A). GRAVITY observations include data from the fringe tracker, which operates at a spectral resolution of $\mathcal{R} = \Delta\lambda/\lambda \sim 22$, as well as the science combiner either in Medium ($\mathcal{R} \sim 500$) or High ($\mathcal{R} \sim 4000$) resolution (Gravity Collaboration et al. 2017). Our observations achieved an angular resolution up to $(\lambda/2B_{\text{max}}) = 1.6$ milliarcseconds (mas) on the longest baselines ($B_{\text{max}} = 130$ m in length), sufficient to spatially resolve the components of MWC 166 A (Gravity Collaboration et al. 2017). The reduction pipeline used was the GRAVITY data reduction pipeline¹ running in the ESOreflex v2.9.1 environment (Freudling et al. 2013). Besides the statistical uncertainties computed by the GRAVITY pipeline, we include 5% and 1° errors, for the visibility and closure phase respectively, to account for calibration uncertainties.

The PIONIER observations covered the H -band (1.59–1.75 μm) and were obtained as part of multiple ESO programmes: 102.C-0701, 104.C-0737 and 106.21JU. These data were recorded over 6 channels at spectral resolution $\mathcal{R} \sim 40$. The reduction pipeline used was pndrs v3.52 (Le Bouquin et al. 2011). We also included published data from the large programme 190.C-0963² (e.g. Lazareff et al. 2017; Kluska et al. 2016), over 3 spectral channels and with a resolution of $\mathcal{R} \sim 15$.

MIRC-X was used in its H -band mode as part of the programme 2020B-M7, using 4 of the 6 CHARA Array telescopes. CHARA’s much longer maximum baseline of 330 m allowed us to probe the object geometry at nearly 3-times higher resolution than possible with VLTI. The MIRC-X v0.9.5 pipeline³ (Anugu et al. 2020, § 4) was used to reduce the data.

A full description of the observations is provided in Table 1. Each observation was calibrated by observing suitable calibrator stars with known uniform disc diameters (UDDs, taken from Bourges et al. 2017), to account for atmospheric absorption and instrument response. The calibrators were also inspected for signatures of binarity to ensure only single stars were observed. In order to improve the (u, v) -coverage, we grouped the individual measurements into epochs. However, this proved to be difficult due to the rapidly-changing orbit of the system. Based on the literature RV orbital period of ~ 183 days (Pogodin et al. 2006), a variation of about one degree in position angle (PA) per day is to be expected. Considering that the PA uncertainties in our binary model fits are on the same order of magnitude as this (see Table 3), each epoch should include data from at most two consecutive nights, ensuring that the relative positions of the two components do not change significantly during each epoch. The observations for which this consolidation was performed are marked accordingly in Table 1.

¹ Available at: <https://ftp.eso.org/pub/dfs/pipelines/instruments/gravity/gravity-pipeline-manual-1.5.4.pdf>

² Taken from the Optical Interferometry DataBase (OiDB), available at: <http://oidb.jmmc.fr>.

³ Available at: https://gitlab.chara.gsu.edu/lebouquj/mircx_pipeline

Table 1: Full list of interferometric observations of MWC 166. Data from programme 190.C-0963 are lacking calibrator information, due to being taken pre-calibrated from the JMMC OiDB.

Date	Programme ID	Array Config	Instrument	$\Delta\lambda/\lambda$	Calibrator(s) used
2013-01-27	190.C-0963(A)	K0-A1-G1-J3	PIONIER	15	-
2013-02-20	190.C-0963(B)	D0-G1-H0-I1	PIONIER	15	-
2017-03-14	098.C-0910(A)	A0-G1-J2-J3	GRAVITY	22 & 4000	HD 49647
2017-04-27 ^a	098.C-0910(A)	A0-G1-J2-J3	GRAVITY	22 & 4000	HD 57087
2017-04-28 ^a	098.C-0910(A)	A0-G1-J2-J3	GRAVITY	22 & 500	HD 49647
2018-01-11	098.C-0910(A)	A0-G1-J2-J3	GRAVITY	22 & 4000	HD 49647
2018-02-06	098.C-0910(A)	A0-G1-J2-J3	GRAVITY	22 & 4000	HD 38117
"	098.C-0910(A)	A0-G1-J2-J3	GRAVITY	22 & 500	HD 55137
2018-11-29 ^a	102.C-0701(B)	A0-G1-J2-K0	PIONIER	40	HD 51914
2018-11-30 ^a	102.C-0701(B)	A0-G1-J2-K0	PIONIER	40	HD 51914
2019-12-15 ^a	104.C-0737(C)	A0-B2-C1-D0	PIONIER	40	HD 51914
2019-12-16 ^a	104.C-0737(C)	A0-B2-C1-D0	PIONIER	40	HD 49741
2019-12-23 ^a	104.C-0737(A)	D0-G2-J3-K0	PIONIER	40	HD 51914
2019-12-24 ^a	104.C-0737(A)	D0-G2-J3-K0	PIONIER	40	HD 51914
2019-12-29	104.C-0737(B)	A0-G1-J2-J3	PIONIER	40	HD 51914
2020-11-18 ^a	2020B-M7	W1-S2-S1-E2	MIRC-X	102	HD 58457
2020-11-19 ^a	2020B-M7	W2-W1-S2-S1	MIRC-X	50	HD 54930
2020-12-13	106.21JU.002	A0-G1-J2-J3	PIONIER	40	HD 45694, HD 54438, HD 51914
2020-12-19	106.21JU.001	D0-G2-J3-K0	PIONIER	40	HD 45694, HD 54438, HD 51914
2020-12-28	106.21JU.003	A0-B2-C1-D0	PIONIER	40	HD 45694, HD 54438, HD 51914

Notes. ^(a) Observations on consecutive days were grouped into one epoch for continuum analysis.

3. Modelling

3.1. Continuum modelling of the system

We fit the interferometric visibility and closure phase data at each epoch using the Exeter in-house geometric modelling pipeline (e.g. Kreplin et al. 2018). As the stellar radii of MWC 166 Aa+Ab are expected to be ~ 0.04 mas at the distance calculated by Kaltcheva & Hilditch (2000), we assume that the stellar photospheres can be modelled as point sources.

Initially, the visibilities and closure phases of MWC 166 A were fitted with the following free parameters: separation (ρ); position angle⁴ of the secondary component from the primary (θ); and the flux contribution of the secondary to the total flux in the model (f_2/f_{tot}). The primary flux contribution was kept fixed

Due to the changes in the f_2/f_{tot} flux ratio, the secondary is at some epochs brighter than the primary in our near-infrared wavelength bands. While there is some variability to the system as a whole over year-length timescales (Pogodin et al. 2006), the relative brightness of the two stars has not been previously recorded, so this was an unexpected finding. In light of this, we restricted θ either to the $[0^\circ, 180^\circ]$ or $[180^\circ, 360^\circ]$ range, where the quadrant was chosen for each epoch to achieve an astrometric orbit that is consistent with the spectroscopic orbit of Pogodin et al. (2006). This was done to ensure that the primary and secondary components of the system were correctly identified at each epoch.

Initially, we did not account for contributions from possible dust emission, consistent with the low measured infrared excess emission in the K -band (Tjin A Dje et al. 2001). The 2-point-source model fits allowed us to derive the astrometry of the two components of the system, but yield a flux ratio that changes significantly between epochs, both in the H - and K -band. These models also consistently overpredicted the visibilities, as can be seen from the red points on Fig. 1, leading to large reduced χ^2

values, in particular on the visibilities (e.g. $\chi_{\text{vis}}^2 > 16$ for the MIRC-X data). In order to reduce this systematic error, we also conducted fits that include extended emission.

3.1.1. Evidence for extended circumbinary disc emission

We tried modelling the extended flux assuming three different geometries: a Gaussian with full-width at half maximum σ , seen under inclination i and a major axis (East of North) position angle Θ_{ext} ; a ring with radius R and a thickness of $0.2R$, seen under inclination i and a position angle Θ_{ext} ; and as over-resolved flux ‘background’ (modelled as a circular Gaussian with $\sigma = 1000$ mas, i.e. filling the field-of-view). The integrated flux contribution of the extended emission component to the total flux in the model is $f_{\text{ext}}/f_{\text{tot}}$, where we define $f_{\text{tot}} \equiv f_1 + f_2 + f_{\text{ext}}$.

For the VLTI epochs, the different geometries for the extended emission returned improved χ^2 values over the 2-point-source model, but no one extended model had consistently smaller χ^2 values over all epochs. Adopting a Gaussian geometry for the extended emission component results in χ_{vis}^2 values ranging from 0.34 to 2.24, while adapting a ring geometry results in $\chi_{\text{vis}}^2 = 0.49\dots 4.65$, and over-resolved flux results in $\chi_{\text{vis}}^2 = 0.57\dots 6.81$. For comparison, the pure point-source model has χ_{vis}^2 between 0.94 and 31.86. Closure phase χ^2 values were found to be almost completely model-independent, with the models returning $\chi_{\text{CP}}^2 < 2.84$ (point-sources), $\chi_{\text{CP}}^2 < 1.62$ (background), $\chi_{\text{CP}}^2 < 1.13$ (Gaussian), $\chi_{\text{CP}}^2 < 1.43$ (ring).

The MIRC-X data probes $\sim 3\times$ higher spatial frequencies than the VLTI data. Data taken over a larger range of spatial frequencies allows us to probe further lobes of the visibility curve, which helps to more reliably distinguish the effects of the extended emission from the sinusoidal binary modulation. Figures 1 and 2 respectively show the resultant model visibilities and closure phases obtained from our geometric models described above, overlaid over the data. While the closure phases are well-

⁴ Defined as East of North

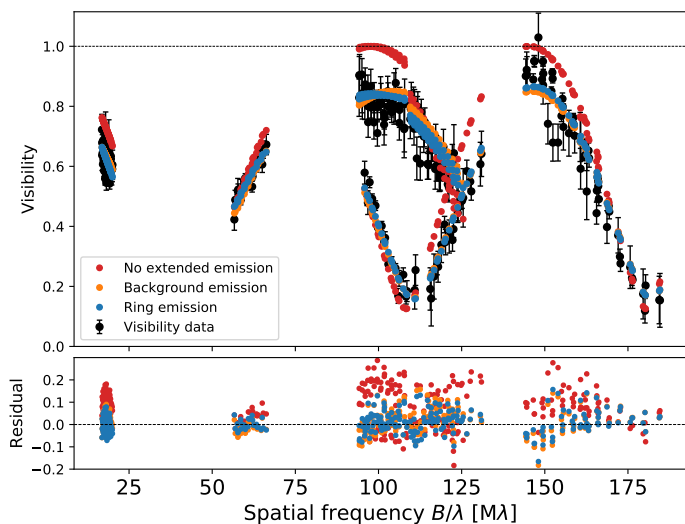


Fig. 1: Visibilities (and associated residuals) of MIRC-X models. At $V \gtrsim 0.6$, the purely point-source model overshoots the observed datapoints substantially.

Table 2: MIRC-X extended emission model comparison.

Model:	No ext. emission	Background	Ring
ρ [mas]	2.87 ± 0.01	2.84 ± 0.01	2.84 ± 0.01
θ [°]	134.3 ± 0.4	131.1 ± 0.3	131.7 ± 0.3
f_2/f_{tot}	0.437 ± 0.012	0.345 ± 0.004	0.344 ± 0.006
R [mas]	-	-	$4.55^{+0.22}_{-0.19}$
i [°]	-	-	55.2 ± 4.0
Θ_{ext} [°]	-	-	$100.6^{+13.1}_{-9.8}$
$f_{\text{ext}}/f_{\text{tot}}$	-	0.150 ± 0.004	0.150 ± 0.005
χ^2_{vis}	16.47	3.27	2.63
χ^2_{CP}	4.28	1.95	2.07

described by the original 2-point-source model independently of any extended flux or lack thereof, for the visibilities this is not the case. The 2-point-source model, represented by the red points on Fig. 1, clearly overpredicts the visibility compared to the other models, especially in the high-visibility regime (where $V \gtrsim 0.6$). The model parameters corresponding to Figs. 1 and 2 are shown in Table 2.

By examining the χ^2 values both for visibility and closure phase in Table 2, it can be seen that the background model provides a significant improvement on the 2-point-source model. A ring profile provides a similar, or even slightly better fit (see Table 2), but introduces 3 additional free parameters while providing only a marginal improvement in the goodness of the fit. We also conducted a fit for a Gaussian model ($\sigma, i, \Theta_{\text{ext}}$) which returned similar χ^2 values to the ring model, but we found that the parameters i and Θ_{ext} did not converge to a value independent of the boundary conditions chosen, while the flux parameters f_2/f_{tot} and $f_{\text{ext}}/f_{\text{tot}}$ were found to be consistent with the background model. As such, we favour the background model over the Gaussian model.

Therefore, we adopt the overresolved background model as geometry for the extended emission for all epochs and instruments, likely representing scattered light from the disc. This minimised the model complexity and degrees of freedom. The relative astrometry was therefore fitted with four free parameters: separation (ρ); position angle of the secondary component

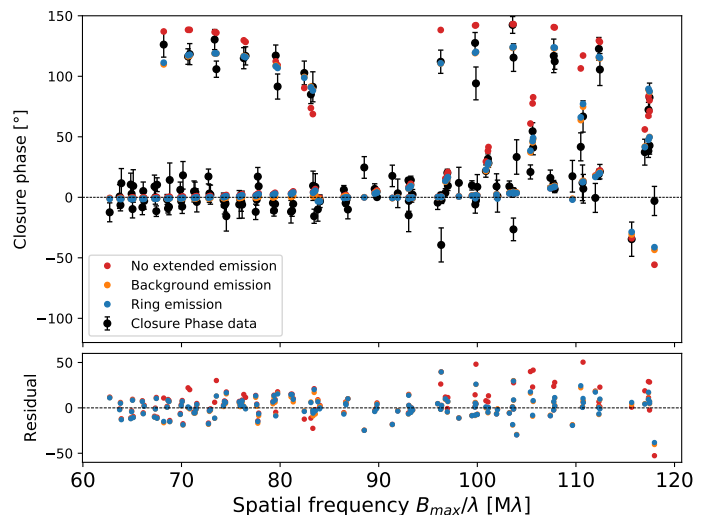


Fig. 2: Closure phases (and associated residuals) of MIRC-X models.

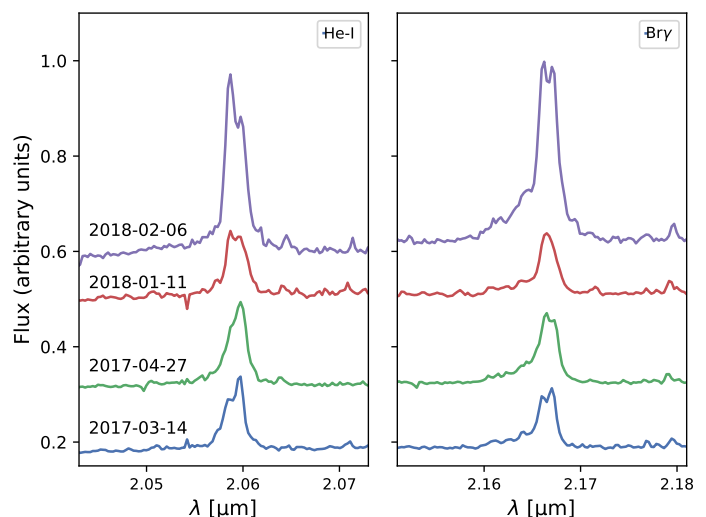


Fig. 3: Continuum-normalised spectra around the He I and Br γ lines. The different epochs have been offset for clarity. Epoch-dependent variations are visible.

from the primary (θ); secondary flux as fraction of the total flux (f_2/f_{tot}) and extended flux as fraction of the total flux ($f_{\text{ext}}/f_{\text{tot}}$).

It is apparent that the relative astrometry of the binary (ρ, θ) does not depend much on whether extended flux is included in the fit. The value of f_2/f_{tot} and $f_{\text{ext}}/f_{\text{tot}}$ change depending on whether extended emission is included in the fit, but is rather independent of the geometry of the emission.

3.2. Modelling of the K-band He I and Br γ lines

For the GRAVITY data, we simultaneously recorded high-resolution data ($\Delta\lambda/\lambda = 4000$) for all epochs, in addition to the low-resolution data used to establish the relative astrometry. As can be seen from MWC 166 A's K-band spectrum, there are strong line features at 2.058 and 2.166 μm (Fig. 3), corresponding to Helium-I and Brackett- γ emission respectively.

In order to model the spectral lines, we used the fitting tool PMOIRE⁵, which is capable of fitting closure phases, differential

⁵ Reference: <https://github.com/amerand/PMOIRE>

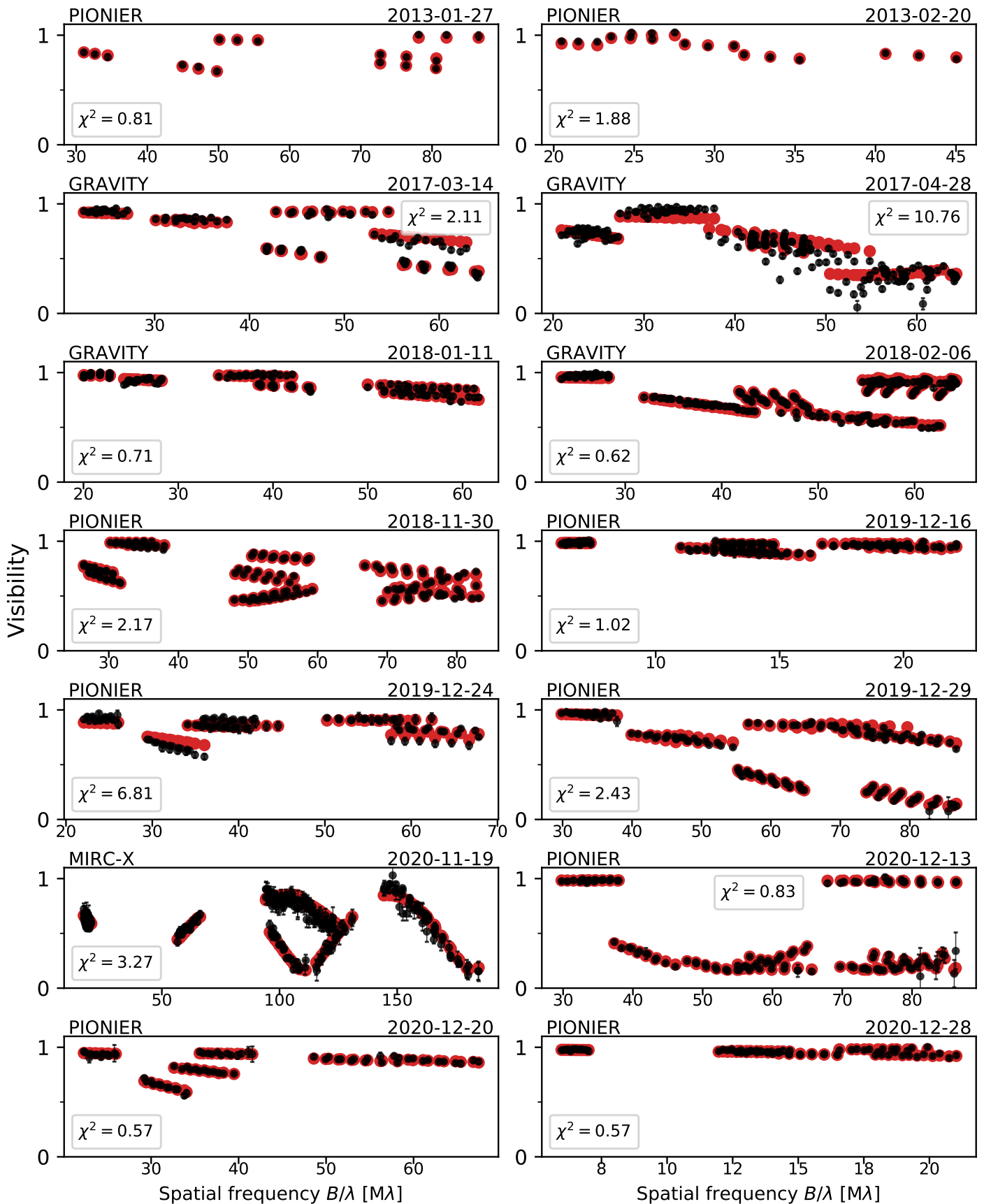


Fig. 4: Observed continuum visibilities (black) and corresponding models (red) plotted against spatial frequency for all epochs. The model fit included extended background emission.

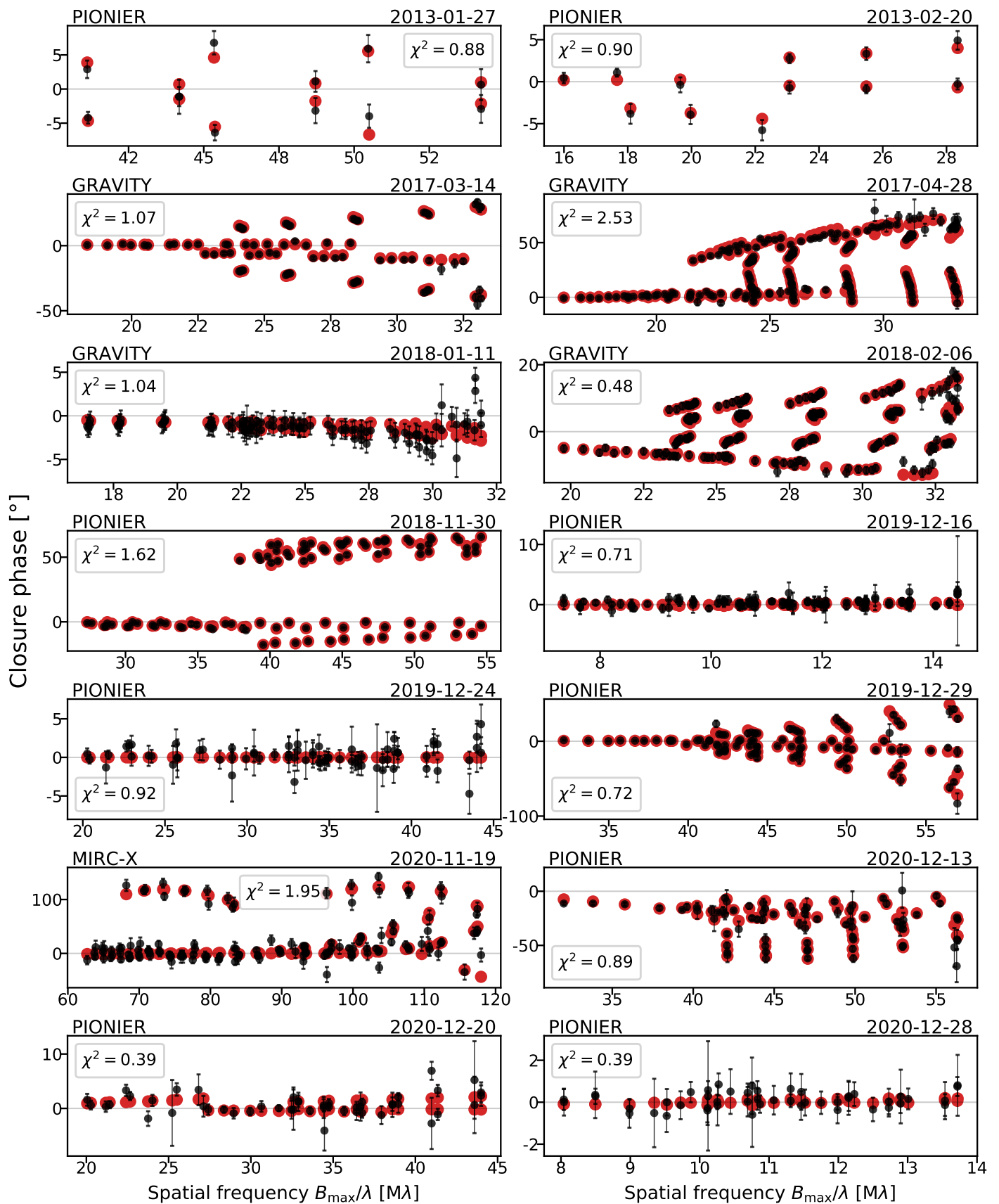


Fig. 5: Observed continuum closure phases (black) and corresponding models (red) plotted against spatial frequency for all epochs. The model fit included extended background emission. The scaling on the vertical axis was adjusted for each epoch.

Table 3: Relative astrometry for MWC 166 Aa+Ab, derived from H - and K -band continuum visibility and closure phase modelling. The model included two point-sources and extended background emission, for a total of four free parameters: separation ρ , position of secondary component θ (East of North), secondary flux f_2/f_{tot} , and extended flux $f_{\text{ext}}/f_{\text{tot}}$.

Epoch	Inst.	ρ [mas]	θ [°]	f_2/f_{tot}	$f_{\text{ext}}/f_{\text{tot}}$	χ_{vis}^2	χ_{CP}^2
2013-01-27	PIONIER	1.50 ± 0.09	309.8 ± 0.3	0.223 ± 0.015	0.021 ± 0.005	0.81	0.88
2013-02-20	"	1.68 ± 0.12	343.5 ± 1.1	0.189 ± 0.021	0.002 ± 0.001	1.88	0.90
2017-03-14	GRAVITY	1.59 ± 0.08	358.7 ± 0.4	0.289 ± 0.003	0.051 ± 0.004	2.11	1.07
2017-04-28 ^a	"	1.90 ± 0.10	47.4 ± 0.2	0.268 ± 0.003	0.116 ± 0.005	10.76	2.53
2018-01-11	"	0.89 ± 0.05	233.3 ± 1.0	0.295 ± 0.013	0.015 ± 0.003	0.71	1.04
2018-02-06	"	1.54 ± 0.08	306.2 ± 0.2	0.274 ± 0.003	0.023 ± 0.002	0.62	0.48
2018-11-30 ^a	PIONIER	2.43 ± 0.12	138.2 ± 0.1	0.271 ± 0.001	0.013 ± 0.002	2.17	1.62
2019-12-16 ^a	"	2.03 ± 0.11	148.1 ± 0.8	0.508 ± 0.005	0.011 ± 0.002	1.02	0.71
2019-12-24 ^a	"	1.34 ± 0.07	154.2 ± 0.6	0.456 ± 0.002	0.087 ± 0.004	6.81	0.92
2019-12-29	"	1.34 ± 0.07	167.5 ± 0.1	0.429 ± 0.001	0.023 ± 0.002	2.43	0.72
2020-11-19 ^a	MIRC-X	2.84 ± 0.14	131.1 ± 0.3	0.345 ± 0.004	0.150 ± 0.004	3.27	1.95
2020-12-13	PIONIER	2.09 ± 0.10	144.6 ± 0.1	0.410 ± 0.001	0.013 ± 0.002	0.86	0.89
2020-12-19	"	1.85 ± 0.09	149.7 ± 0.2	0.422 ± 0.008	0.035 ± 0.002	0.72	1.03
2020-12-28	"	1.53 ± 0.11	162.4 ± 1.3	0.675 ± 0.058	0.018 ± 0.005	0.57	0.39

Notes. ^(a) Data combines two days of observation modelled simultaneously, as defined in table 1.

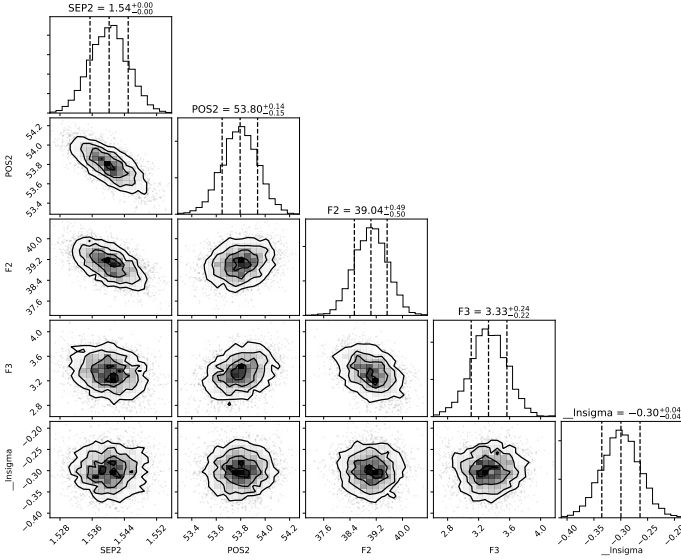


Fig. 6: Corner plot showing the possible correlations between free parameters (ρ , θ , $F_2 = 100 \cdot f_2/f_{\text{tot}}$ and $F_3 = 100 \cdot f_{\text{ext}}/f_{\text{tot}}$ respectively) for epoch 2018-02-06 of the continuum GRAVITY data, where the model fit included extended background emission.

phases, differential visibilities, and line spectra simultaneously, both over the continuum and over specific spectral windows.

After finding the continuum geometry of the system for each epoch (Sect. 3.1.1), we introduced new model components to fit the He I and Br γ lines individually, using geometries of varying complexity. We initially used a single Gaussian of full-width-at-half-maximum (FWHM) $\sigma = 0.1$ mas and left the position of the line-emitting region as a free parameter. At all epochs, this resulted in only very small spatial displacements from the origin, suggesting the primary component is responsible for the majority of the emission in the system. However, this singular emission zone near the primary is perhaps too simplistic a model. If we examine the flux intensity of the two lines (Fig. 3), there are indications of time-dependent variability, as well as signs of

double-peaked lines at several epochs. This could imply that the emission originates from both stars, or it could be a signature of the gas kinematics. Furthermore, the differential phases over the spectral lines show signatures of rotating emission which are not accurately modelled by the single-Gaussian model. These features would be most naturally explained by a circumprimary disc.

3.2.1. Circumprimary gas disc model

The circumprimary disc model we used is based on the model described in Frost et al. (2022), which was used to model the binary system HR 6819. The model is comprised of several components, and has 12 free parameters which describe the entirety of the system.

Firstly, the stars themselves are modelled as uniform discs with diameters corresponding to twice the stellar radii we obtained from our continuum fit (see Sect. 4.4), and the secondary component is given a displacement from the primary's position at the origin, as well as a continuum flux f_2/f_1 , while the primary flux is fixed to $f_1 \equiv 1$.

The line emission is subsequently modelled to be originating from two regions, one blue-shifted and the other red-shifted, to represent the approaching and receding part of a rotating disc (labelled B and R respectively). Each of these components was given its own spatial displacement (x_i, y_i) , with the size of the emitting region following a Gaussian profile with FWHM $\sigma_i = \frac{1}{2} \sqrt{x_i^2 + y_i^2}$. We additionally modelled the line components in the spectral domain. Each component is given a flux profile $F_i = f_i + F_L$, consisting of a Lorentzian component F_L which was kept equal for both wings, and a flat component f_i , accounting for the differences in line strength between the components (which can be seen to vary by epoch in Fig. 3). Each line wing is centred on a wavelength which is displaced from the central line wavelength λ_0 , such that $\lambda_B = (\lambda_0 - \Delta\lambda)$ and $\lambda_R = (\lambda_0 + \Delta\lambda)$.

The resultant fitted parameters of the model described above are presented for all GRAVITY epochs in Sect. 5. The model is fitted simultaneously to the telluric-corrected spectrum, closure phase, differential phase, and differential visibility.

4. Results: Orbital solution and mass/distance constraints

4.1. Binary astrometry and orbital fit

The parameters of our best-fit continuum model with background component are listed in Table 3. The model visibilities that correspond to the best-fit model are shown in Fig. 4, while closure phases are shown in Fig. 5. Our modelling script makes use of Markov Chain Monte Carlo module *emcee* (Foreman-Mackey 2016) to explore the parameter space and obtain error estimates from the posterior probability distribution. We show the corner plot for a representative epoch (2018-02-06) in Fig. 6. An important source of systematic uncertainty that affects primarily the derived separations is the wavelength calibration, and we account for this by including a systematic uncertainty of 5% (Gallenne et al. 2018) for the separations listed in Table 3.

Using the relative astrometry for each epoch, we fitted a Keplerian orbit using the standard Campbell elements: P = orbital period; T_0 = epoch of periastron passage; a_1 = semi-major axis of primary component; i = orbital inclination (to line of sight); e = eccentricity; Ω = longitude of ascending node; ω = longitude of periastron; K_1 = orbital curve semi-amplitude of primary component; V_0 = RV of the system's centre of mass.

We used two fitting approaches:

ORBITX code: This code⁶ (Tokovinin 1992) fits orbits using both astrometric and RV data simultaneously. We modified the ORBITX code to account for uncertainties in both ρ and θ , a feature absent from the original code, which only uses uncertainties on ρ .

Grid-search algorithm: We used the grid-search algorithm developed by Kraus et al. (2009) to construct a grid of orbital solutions in the P , T_0 , and e parameter space, where the remaining elements a , i , Ω , ω are determined from the Thiele-Innes elements. We explored the parameter space around $P = 0.480\dots 1.100$ yr, $T_0 = 2019.5\dots 2020.5$ yr (step sizes of 0.001 yr), and $e = 0.100\dots 0.600$ with a step size of 0.001, and selected the solution with the lowest combined residuals in RV and astrometry. We then repeated the process with smaller step-sizes around the initial solution (a factor of ten for all parameters, = 0.0001 yr, 0.0001 yr, 0.0001 respectively for P , T , e), in order to increase precision. Uncertainties were calculated by examining the χ^2 curve for each parameter.

The best-fit orbit solutions found with these methods are listed in columns (3), (4) of Table 4, and are overplotted on the data in Figs. 7 and 8. Both the orbits provide a very good fit to the existing data, and provide similar results for all parameters. This is despite a substantial portion of the orbit still lacking astrometric observations. We adopt the orbit from column (3) when discussing derived quantities in the subsequent sections.

4.2. Comparison to RV orbit

Corporon & Lagrange (1999) and Pogodin et al. (2006) derived orbits for MWC 166 A from the RV data, with the more recent of the two being a refinement including additional RV points. The orbital parameters for this RV orbit are shown in column (2) of Table 4. Our spectroscopic+astrometric orbital solutions differ substantially from the earlier RV-only orbit. The most notable difference is in the orbital period, which we calculated as almost exactly twice the length of Pogodin et al. (2006)'s orbit. This doubling of the period was only discernible thanks to our astrometric data, as using the radial velocities alone provides an

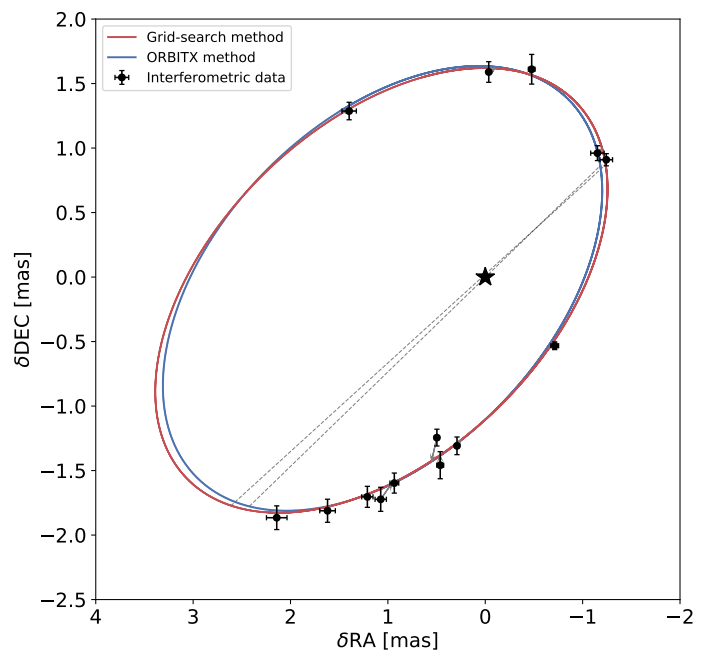


Fig. 7: Astrometric orbit solutions derived using both the ORBITX code (blue line) and grid-search code (red line). The primary star is kept fixed at the origin, and the x - and y -axes show displacement in right ascension and declination respectively. The dotted lines connect the ascending and descending nodes of each orbit.

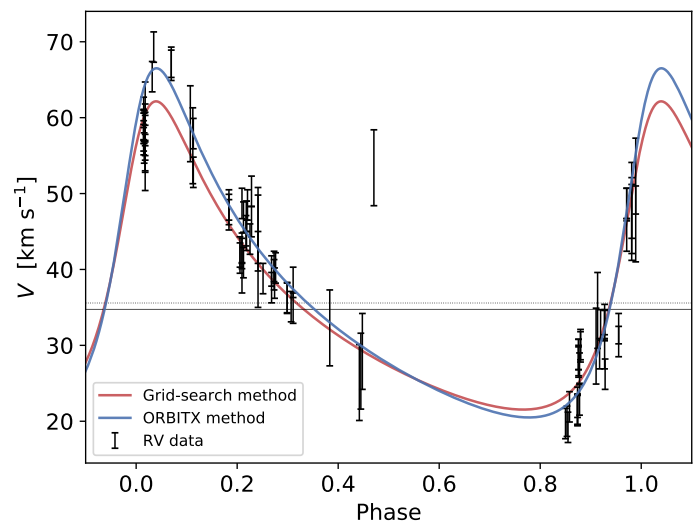


Fig. 8: Radial velocity measurements of MWC 166 A taken in the period 1994–2005 plotted against orbital phase. The blue and red fitted curves correspond to the orbits specified in columns (3) and (4) of table 4, respectively. The black dotted line shows the velocity of the system's centre of mass (V_0) for the grid-search method, and the solid grey line shows V_0 for the ORBITX orbit.

equally good fit to both orbits. We also found the orbit to be much more elliptical than previously thought, with its eccentricity of 0.498 ± 0.003 being much larger than that of the RV orbit ($e = 0.28 \pm 0.03$). A newly determined parameter from our orbit is the inclination, with a value of $i = 53.6 \pm 0.3^\circ$.

⁶ Available at: <https://zenodo.org/record/61119>

Table 4: Orbital parameters for MWC 166 A. Column (2) gives the RV fit obtained by Pogodin et al. (2006). Columns (3) and (4) give the best-fit orbital solution including both RV data and the astrometry data, using the ORBITX and the grid-search methods respectively. These solutions were derived using the background geometric model described in Sect. 3.1.1.

Parameter (1)	RV only (2)	ORBITX orbit (3)	Grid-search orbit (4)
P [yr]	0.50296 ± 0.00027	1.0067 ± 0.0001	1.0066 ± 0.0002
P [days]	183.70 ± 0.10	367.69 ± 0.04	367.65 ± 0.07
T_0 [yr]	1993.3581 ± 0.0078	2020.0722 ± 0.0003	2020.0713 ± 0.0010
a_1 [mas]	-	2.6122 ± 0.0385	2.684 ± 0.008
i [°]	-	53.62 ± 0.32	55.27 ± 0.11
$a_1 \sin i$ [mas]	2.15 ± 0.07^a	-	-
e	0.28 ± 0.03	0.498 ± 0.001	0.492 ± 0.003
Ω [°]	-	306.3 ± 0.2	304.9 ± 0.2
ω [°]	263.8 ± 6.6	313.8 ± 0.2	315.6 ± 0.5
K_1 [km s ⁻¹]	18.6 ± 0.7	20.3 ± 0.4	20.3 ± 0.4
V_0 [km s ⁻¹]	44.2 ± 0.5	35.3 ± 0.3	34.7 ± 0.3
$M_{\text{tot}} [M_{\odot}]^b$	-	17.05 ± 2.70	18.52 ± 2.81

Notes. ^(a) Pogodin et al. (2006) returns $a \sin i = 60 \pm 2 R_{\odot}$. A conversion to milliarcseconds has been made to allow better comparison with the calculated semi-major axis and inclination. The distance used was 990 pc.

^(b) Mass calculated for $d = (990 \pm 50)$ pc.

4.3. Dynamical system mass

According to Kepler’s third law, the period of an orbit P is proportional to the cube of the semi-major axis of the orbit a . Using the usual angular diameter-distance relation a [au] = a ["] $\times d$ [pc], we can show the dependence of the total system mass $M_{\text{tot}} \equiv (M_1 + M_2)$ (in solar masses) on distance d (in parsecs), where G is the gravitational constant and $M_{1,2}$ the masses of the two stars:

$$M_{\text{tot}} = \frac{4\pi a^3 \mathcal{Z}}{GP^2} d^3, \quad (1)$$

where $\mathcal{Z} = 1684.14 \text{ m}^3 M_{\odot}^{-1}$ is a constant introduced to account for the change in units from au to metre, and from kg to M_{\odot} . In the above equation, the total mass is also known as the ‘dynamical mass’, signifying it is derived from fitting the dynamical orbit of the system. Since $M_{\text{tot}} \propto d^3$, a reliable distance value is needed to obtain rigorous mass estimates.

Unfortunately, there are several conflicting distance estimates for this system in the literature. As mentioned in Sect. 1, photometrically calculated distances have placed MWC 166 at a distance of ~ 1 kpc. Parallax observations have corroborated the photometric distances for a majority of the other individual members of CMaOB1, but are not consistent in the case of MWC 166. Hipparcos (ESA 1997) measured a distance of 247 ± 82 pc, while Gaia Data Release 2 (DR2) parallaxes correspond to an even shorter distance of 131_{-13}^{+16} pc (Bailer-Jones et al. 2018) – roughly ten times closer than the ~ 1 kpc to its parent association. This discrepancy can likely be explained by the binarity of the system, as DR2 does not solve for source multiplicity. Indeed, the recent release of preliminary results from Gaia EDR3 has brought the parallax distance to MWC 166 closer to the photometric distance values, albeit with very large uncertainties ($d \sim 1600 \pm 700$ pc, Bailer-Jones et al. 2021). Our Keplerian mass-distance relation (Eq. 1) shows that distances of $\lesssim 650$ pc correspond to masses of $M_{\text{tot}} < 5 M_{\odot}$, clearly below the mass threshold for MWC 166 Aa’s spectral type of B0III (Fairlamb et al. 2015). Conversely, the photometric distances offer more physically realistic values – the most recent distance estimate of 990 ± 50 pc returns a system mass of $M_{\text{tot}} = 17.1 \pm 2.7 M_{\odot}$, which is also in agreement with the prediction of 20–25 M_{\odot} by

Pogodin et al. (2006). Additionally, any parallax distances are unreliable due to having been calculated with the assumption of a six-month orbit, which we have shown is too short by a factor of two. In light of these points, in this work we have treated the photometric distances preferentially. We have therefore taken the literature distance to MWC 166 to be the most recent photometric distance, 990 ± 50 pc (Kaltcheva & Hilditch 2000).

4.4. From combined mass to individual masses and other properties

Our full orbital solution allows us to constrain model-independent individual masses for the first time. If the system’s orbital period (P), eccentricity (e) and inclination (i) are known, as well as the RV semi-amplitude of the primary component (K_1), it is possible to calculate the binary mass function f (e.g. Boffin 2012; Curé et al. 2015):

$$f \equiv \frac{K_1^3 P (1 - e^2)^{3/2}}{2\pi G} = \frac{(M_2 \sin i)^3}{M_{\text{tot}}^2}, \quad (2)$$

which equates the mass of the secondary component to the other elements. Rearranging for M_2 gives:

$$M_2 = \frac{1}{\sin i} \left[\frac{K_1^3 P (1 - e^2)^{3/2}}{2\pi G} \cdot M_{\text{tot}}^2 \right]^{1/3}, \quad (3)$$

and the mass of the primary can therefore be trivially found through $M_1 = M_{\text{tot}} - M_2$.

Using this method we determined the masses of MWC 166 Aa and MWC 166 Ab as $M_1 = (12.19 \pm 2.18) M_{\odot}$ and $M_2 = (4.90 \pm 0.52) M_{\odot}$, respectively. Our M_{dyn} measurements for both components were used to derive the remaining stellar parameters, and their respective confidence bounds, from theoretical evolution tracks. We used CMD 3.6⁷ to generate a Solar metallicity ($Z = 0.0152$) isochrone table from PARSEC 1.2S (Bressan et al. 2012; Chen et al. 2014, 2015; Tang et al. 2014; Marigo et al. 2017; Pastorelli et al. 2019).

⁷ <http://stev.oapd.inaf.it/cgi-bin/cmd>

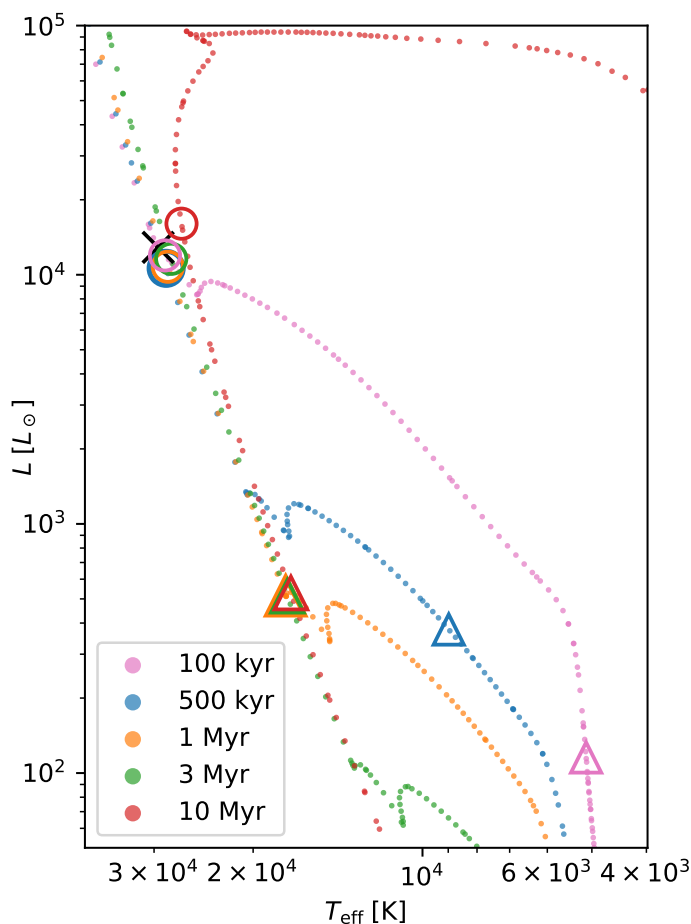


Fig. 9: HR diagram showing PARSEC 1.2S isochrone tracks for each age. Superimposed are the interpolated L , T_{eff} values for the primary star (large circles) and secondary star (triangles), for all ages. The black cross shows the location of the primary’s parameters as determined by Fairlamb et al. (2015).

The evolutionary status of MWC 166 A has not been conclusively established. Analysis of the spatial distribution of O- and B-type stars in its parent OB association, CMa OB1/R1, resulted in an estimate for its age of $\sim 3 \times 10^6$ yr (Clariá 1974). At this age, MWC 166 Aa is likely already onto the main sequence, while MWC 166 Ab might still be in its pre-main-sequence stage (Tjin A Dje et al. 2001). Later work by Herbst & Assoua (1977) showed that CMa OB1/R1’s main stars are located on the rim of an expanding shell of neutral hydrogen, consistent with star formation being triggered by a supernova within the last ~ 500 kyr. Due to the uncertain age of the system, we selected these two potential ages, as well as a reasonable intermediate age (1×10^6 yr), upper bound (1×10^7 yr), and lower bound (1×10^5 yr). Then, for each of the estimated ages, we drew an isochrone of an appropriate age from the CMD table and performed a quadratic interpolation over the mass points within it to find the value for each parameter that corresponds to M_{dyn} at the given age. This process was repeated for the upper and lower bounds on M_{dyn} to find the confidence bounds for each parameter at the given age. Our estimates for the stellar parameters using this method are presented in Table 5. Figure 9 shows the isochrones for each age estimate plotted on a Hertzsprung-Russell diagram of $\log(L)$ vs $\log(T_{\text{eff}})$, as well as the interpolated values for the primary and secondary components as large circles and triangles, respectively.

Table 5: PARSEC 1.2S / COLIBRI S₋₃₇ models of each component of MWC 166 A. Isochrones were selected at five representative ages including reasonable lower and upper bounds, with stellar age parameters corresponding to the dynamical masses of each component. The isochrones assume Solar metallicities and that the stars are coeval.

Parameter	MWC 166 Aa	MWC 166 Ab
$M_{\text{dyn}} [M_{\odot}]$	12.19 ± 2.18	4.90 ± 0.52
Age [yr]	1.0×10^5	
$L [L_{\odot}]$	$(1.20^{+0.53}_{-0.31}) \times 10^4$	$(1.15^{+0.39}_{-0.24}) \times 10^2$
$R [R_{\odot}]$	$4.43^{+0.11}_{-2.03}$	$13.66^{+1.80}_{-1.31}$
$T_{\text{eff}} [\text{K}]$	$28\,700^{+2400}_{-6600}$	$5\,120^{+60}_{-40}$
$\log(g)$	$4.23^{+0.02}_{-0.41}$	$2.85^{+0.04}_{-0.06}$
Age [yr]	5.0×10^5	
$L [L_{\odot}]$	$(1.06^{+0.67}_{-0.49}) \times 10^4$	$(3.77^{+8.01}_{-2.72}) \times 10^2$
$R [R_{\odot}]$	$4.21^{+0.44}_{-0.48}$	$8.02^{+3.70}_{-1.17}$
$T_{\text{eff}} [\text{K}]$	$28\,600^{+2200}_{-2500}$	$9\,000^{+7300}_{-2900}$
$\log(g)$	4.27 ± 0.02	$3.32^{+0.58}_{-0.21}$
Age [yr]	1.0×10^6	
$L [L_{\odot}]$	$(1.08^{+0.70}_{-0.50}) \times 10^4$	$(5.13^{+2.23}_{-1.72}) \times 10^2$
$R [R_{\odot}]$	$4.30^{+0.48}_{-0.50}$	$2.46^{+0.44}_{-0.15}$
$T_{\text{eff}} [\text{K}]$	$28\,400^{+2100}_{-2500}$	$17\,500^{+1100}_{-2900}$
$\log(g)$	4.25 ± 0.02	$4.34^{+0.19}_{-0.01}$
Age [yr]	3.0×10^6	
$L [L_{\odot}]$	$(1.16^{+0.80}_{-0.55}) \times 10^4$	$(5.13^{+2.23}_{-1.72}) \times 10^2$
$R [R_{\odot}]$	$4.59^{+0.58}_{-0.59}$	2.50 ± 0.16
$T_{\text{eff}} [\text{K}]$	$28\,000^{+2100}_{-2500}$	$17\,400^{+1000}_{-1100}$
$\log(g)$	4.20 ± 0.03	4.33 ± 0.01
Age [yr]	1.0×10^7	
$L [L_{\odot}]$	$(1.60^{+1.51}_{-0.86}) \times 10^4$	$(5.28^{+2.39}_{-1.79}) \times 10^2$
$R [R_{\odot}]$	$5.87^{+1.91}_{-1.22}$	$2.61^{+0.20}_{-0.19}$
$T_{\text{eff}} [\text{K}]$	$26\,800^{+700}_{-1900}$	$17\,100^{+1000}_{-1100}$
$\log(g)$	$3.98^{+0.12}_{-0.17}$	4.29 ± 0.02

From Fig. 9, it can be seen that, at the ages of 500 kyr, 1 Myr and 3 Myr, the primary star is on the main sequence, with negligible variations in parameters between these ages. At the upper bound age of 10 Myr, the primary is in the process of beginning to evolve beyond the main sequence. Conversely, it is clear from the HR diagram that the secondary component is predicted to be on the main sequence for all ages save the youngest, where it is still in its protostellar stage. Also on Fig. 9 is shown the location of the primary as calculated by Fairlamb et al. (2015), which appears to agree with all ages except the upper bound of 10 Myr. In Sect. 6.4, we generalise this process to all generated isochrones to attempt to constrain the age of the system.

5. Results: Modelling the gas distribution & kinematics in the He I and Br γ line

The circumprimary disc model described in Sect. 3.2 produces an excellent fit to the data at all epochs.

Figure 10 shows the results of the fit for the epoch 2017-03-14, where panel (a) shows the spectra, closure phases, differential phases, and visibilities measured with GRAVITY overplotted with prediction from the best-fit model. The three left-most plots in panel (b) show synthetic images computed from the best-fit model for three representative wavelengths. The central panel shows the brightness distribution at λ_0 , while on the left- and right-hand sides of this, the wavelength is red-shifted and blue-shifted respectively, by a factor of $\lambda_0 \pm 3\Delta\lambda$. The right-most panel of the figure shows the flux contribution of each synthetic model component.

The line modelling results for all epochs (analogously to Fig. 10) are shown in the Appendix, and the findings are summarised in Table 6, for both spectral lines of interest.

The results show substantial evidence of line emission being localised around the primary star, consistent throughout all four GRAVITY epochs. The red-shifted component (R) is displaced consistently towards the north-west of the primary star, while the blue-shifted component (B) is located south-east of the primary. The displacement of the two components from the star is generally (~ 0.25 mas). The average displacement for He I was found to be $(10.5 \pm 0.4) R_1$, and for the Br γ this was $(11.5 \pm 0.4) R_1$. The derived values for each epoch can be seen in column (5) of Table 7. The relative intensities of the *B* and *R* components also seem to be variable by epoch and by spectral line. From columns (3), (4) of Table 7, it can be seen that, for the He I line, the red wing contributes 60% of the flux for the first two epochs, a similar level of intensity as the blue wing during the latter two epochs. On the other hand, the Br γ line flux tends to be more equally distributed between the two components, apart from in the epoch 2018-02-06, where the blue component is substantially stronger. The emission of the red- and blue-shifted line wing are displaced along an average position angle of $134.0 \pm 1.1^\circ$, indicating that this is the sky-projected position angle of the major-axis of the rotating disc. Accordingly, the rotation axis of the disks, and likely also the primary star, is oriented along position angle $44.0 \pm 1.1^\circ$ on sky.

6. Discussion

6.1. Evidence for circumbinary dust

Our interferometric observations in the continuum allow us to quantify the excess emission through our visibility fit (Sect. 3.1.1), where we find that $\sim 2\%$ and $\sim 5\%$ of the excess emission are associated with extended flux in the *H*-band and *K*-band, respectively. The *H*-band observations also show ‘spikes’ in the extended flux contribution in the epochs 2019-12-24 and 2020-11-19, with $f_{\text{ext}}/f_{\text{tot}}$ contributing up to 15% of the total flux for these epochs. The geometry of the extended dust is still poorly constrained, but our modelling shows the emission originates from scales at least twice larger than the binary separation vector (for a ring model), but likely even larger (for a Gaussian or background flux model; Table 2 and Sect. 3.1.1). This is comparable to the dynamical truncation radius predicted by Artymowicz & Lubow (1994) for circular binaries ($\sim 1.7a$).

The expected Silicate dust sublimation radius (R_s) can be estimated with

$$R_s = 1.1 \sqrt{Q_R} \left(\frac{L}{1000 L_\odot} \right)^{1/2} \left(\frac{T_s}{1500 \text{ K}} \right)^{-2} \text{ au}, \quad (4)$$

where L is the bolometric luminosity of the star(s) irradiating the disk and T_s is the dust sublimation temperature (Monnier

Table 6: Model parameters corresponding to the best-fit PMOIRÉ circumprimary disc line models, for both spectral lines of interest, for each GRAVITY epoch (Sect. 5).

Epoch	2017-03-14			2017-04-27			2018-01-11			2018-02-06		
	He I	Br γ		He I	Br γ		He I	Br γ		He I	Br γ	
ρ [mas]	1.67 \pm 0.01	1.65 \pm 0.01		1.98 \pm 0.01	1.98 \pm 0.01		0.86 \pm 0.02	0.90 \pm 0.02		1.59 \pm 0.01	1.56 \pm 0.01	
θ [°]	357.4 \pm 0.3	357.8 \pm 0.3		42.3 \pm 0.3	42.0 \pm 0.2		238.1 \pm 1.1	238.9 \pm 1.0		307.8 \pm 0.2	307.3 \pm 0.2	
f_2	0.414 \pm 0.004	0.359 \pm 0.003		0.457 \pm 0.004	0.402 \pm 0.002		0.318 \pm 0.025	0.240 \pm 0.016		0.440 \pm 0.007	0.399 \pm 0.006	
x_B [mas]	0.212 \pm 0.017	0.192 \pm 0.015		0.242 \pm 0.034	0.255 \pm 0.031		0.114 \pm 0.016	0.223 \pm 0.022		0.175 \pm 0.013	0.161 \pm 0.013	
y_B [mas]	-0.118 \pm 0.017	-0.184 \pm 0.012		-0.226 \pm 0.028	-0.118 \pm 0.024		-0.091 \pm 0.023	-0.076 \pm 0.036		-0.052 \pm 0.011	-0.123 \pm 0.011	
σ_B [mas]	0.121	0.133		0.166	0.141		0.073	0.118		0.091	0.102	
f_B	0.712 \pm 0.015	0.633 \pm 0.015		0.668 \pm 0.026	0.497 \pm 0.023		0.533 \pm 0.016	0.289 \pm 0.020		0.945 \pm 0.016	0.643 \pm 0.015	
x_R [mas]	-0.155 \pm 0.011	-0.190 \pm 0.013		-0.168 \pm 0.021	-0.208 \pm 0.021		-0.048 \pm 0.017	0.040 \pm 0.020		-0.130 \pm 0.015	-0.053 \pm 0.020	
y_R [mas]	0.168 \pm 0.009	0.135 \pm 0.011		0.188 \pm 0.017	0.202 \pm 0.017		0.184 \pm 0.026	0.244 \pm 0.032		0.241 \pm 0.014	0.243 \pm 0.019	
σ_R [mas]	0.114	0.117		0.126	0.145		0.095	0.124		0.137	0.124	
f_R	1.074 \pm 0.014	0.688 \pm 0.013		1.009 \pm 0.021	0.664 \pm 0.017		0.425 \pm 0.014	0.309 \pm 0.016		0.603 \pm 0.014	0.326 \pm 0.012	
F_L	1.045 \pm 0.016	1.046 \pm 0.022		1.231 \pm 0.031	1.340 \pm 0.041		1.150 \pm 0.026	1.386 \pm 0.048		1.051 \pm 0.018	1.330 \pm 0.030	
λ_0 [μm]	2.0590	2.1665		2.0593	2.1667		2.0593	2.1667		2.0592	2.1667	
$\Delta\lambda$ [μm]	0.617 \pm 0.005	0.577 \pm 0.006		0.568 \pm 0.009	0.558 \pm 0.011		0.578 \pm 0.008	0.422 \pm 0.016		0.606 \pm 0.006	0.576 \pm 0.011	
χ^2	2.55	2.37		4.18	3.07		2.22	1.95		3.53	3.04	

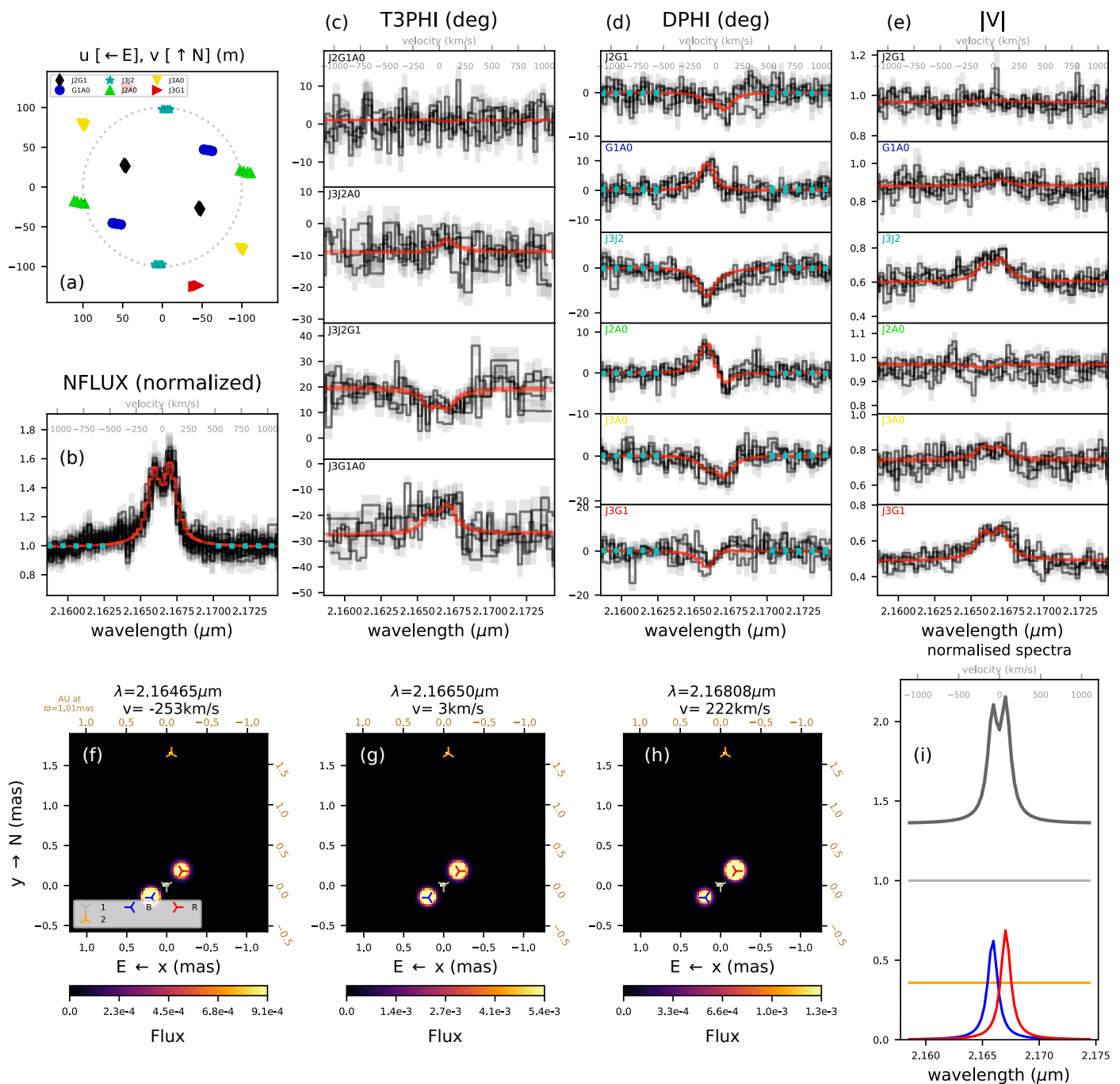


Fig. 10: Results of the Br γ line modelling, for the epoch 2017-03-14. **(a)**: The (u, v) -coverage for the observations associated with the epoch, coloured by baseline pair. **(b)**: Telluric-corrected normalised flux (labelled NFLUX, black lines), overplotted with flux in the best-fit model (red line). **(c)**, **(d)**, **(e)**: Data from each GRAVITY exposure (black lines), overplotted with quantities computed from best-fit model (red lines). The observables are closure phase for each telescope triplet (T3PHI), differential phase for each baseline (DPHI), and visibility for each baseline ($|V|$), respectively. **(f)**, **(g)**, **(h)**: brightness distribution corresponding to the best fit, for three representative wavelengths. **(i)**: Synthetic line strengths and profiles for the two spectral components in the model (red and blue), in addition to the monochromatic continuum flux associated with the primary component (silver) and the secondary component (gold). The parameters corresponding to the fits can be found in Table 6.

& Millan-Gabet 2002). $Q_R \equiv Q_{\text{abs}}(T_*)/Q_{\text{abs}}(T_s)$ is the ratio of dust absorption efficiencies for radiation for the incident and re-emitted field, which we fix to $Q_R = 1$ in order to estimate the rim location for large μm -sized dust grains. The above equation has several simplifications compared to the physical system, chief among which is the assumption of a single star rather than a binary. While dust sublimation radii have been calculated for

binary systems (e.g. Nagel et al. 2010), dynamical interactions cause the inner dust rim to be at a larger radius than R_s . A detailed calculation is therefore outside the scope of this work, but equation 4 can still give an order-of-magnitude estimate for the minimum dust inner rim radius of the circumbinary disc, assuming a luminosity equivalent to that of the two components combined. Substituting the sum of the luminosity values from the

Table 7: Columns (3) and (4): relative strengths of the red and blue wings of the respective spectral line. Uncertainties are 0.01 for all values in these columns. Columns (5) and (6): radius of line emission centre, averaged from the red and blue wings, given respectively in units of milli-arcseconds, and the primary star’s radius at 3 Myr (see Table 5). Column (7) shows the estimated rotational axis of the primary star.

Epoch (1)	Line (2)	f_R/f_{R+B} (3)	f_B/f_{R+B} (4)	$\bar{\rho}_{\text{line}}$ [mas] (5)	$\bar{\rho}_{\text{line}}$ [R_1] (6)	θ_{rot} [°] (7)
2017-03-14	He I	0.60	0.40	0.24 ± 0.02	11.2 ± 0.9	37.9 ± 2.4
	Br γ	0.52	0.48	0.25 ± 0.01	11.6 ± 0.5	39.9 ± 2.1
2017-04-27	He I	0.60	0.40	0.29 ± 0.03	13.5 ± 1.4	45.0 ± 4.0
	Br γ	0.57	0.43	0.29 ± 0.03	13.5 ± 1.4	34.7 ± 3.3
2018-01-11	He I	0.44	0.56	0.17 ± 0.02	7.9 ± 0.9	59.0 ± 5.0
	Br γ	0.52	0.48	0.24 ± 0.03	11.2 ± 1.4	60.0 ± 5.0
2018-02-06	He I	0.39	0.61	0.23 ± 0.01	10.7 ± 0.5	43.9 ± 2.5
	Br γ	0.34	0.66	0.23 ± 0.02	10.7 ± 0.9	59.7 ± 3.2

central age estimate of 1 Myr in Table 5 gives $R_s = 2.6$ au, 4.6 au and 7.1 au for dust sublimation temperatures of 2000 K, 1500 K and 1200 K, respectively. This suggests that individual dusty circumstellar discs are likely not present in the MWC 166 A system. Due to the calculated semi-major axis of the orbit being comparable to the smallest of the above estimates ($a_1 = 2.61$ au at $d = 990$ pc), it is expected that substantial individual dusty discs around each of the components are not capable of surviving for extended periods of time due to dynamical interactions (e.g. Mathieu 1994). Accordingly, we associate the extended continuum emission with a circumbinary disc component instead of circumstellar disc component.

6.2. Evidence for variable extinction or circumstellar material

The relative flux contribution of the two point sources in our model was found to be variable, especially in the H -band continuum. The flux associated with the secondary appears to increase around phase ~ 0.9 , and was found to be as bright as the primary at one epoch (2019-12-24) and even brighter than the primary at two epochs (2019-12-16 and 2020-12-28). These latter two epochs were both taken on the compact AT configuration, and returned visibilities very close to unity – as well as closure phases close to zero – at all probed baselines (See Figs. 4 and 5). This, and the more limited (u, v)-coverage caused by the shorter baselines, can result in ambiguities in the model (Anthonioz et al. 2015). To rule this out, we repeated the modelling for these two epochs while restricting the secondary to a maximum brightness of 100% of the primary. We then repeated the astrometric fit, and found it to be incompatible with any physical orbit when considered with the other points. This means that the secondary’s increase in relative H -band brightness to outshine the primary at the epochs 2019-12-16 and 2020-12-28 is the only solution which agrees with the Keplerian orbit of the objects.

Since these two points are at very similar orbital phases (0.88 and 0.91 respectively), we argue that this variability could be a result of the dynamical interaction of the secondary with the circumbinary disc, possibly through variable extinction, where the line-of-sight extinction changes towards one of the stars due to rearrangements in the circumbinary disc. In addition, our point-source flux estimate (f_2/f_1) might contain emission contributions from circumstellar gas or dust, in particular as the binary separation is still comparable to our interferometric beam size. Therefore, the observed f_2/f_1 brightness increase might correspond to an increase in excess emission near the location of the secondary as it approaches periastron, either through an accretion burst onto the secondary or from a hot spot at the inner

edge of the circumbinary disc caused by the additional heating from the secondary. Indeed, SPH simulations of young, eccentric close binaries with circumbinary discs such as those by Dunhill et al. (2015, for HD 104237) and Muzerolle et al. (2019, for DQ Tau), have suggested that dynamical interactions can cause a differential rate of accretion depending on the orbital phase, with the highest accretion peak occurring during the 10 – 20% of the orbit preceding periastron. The observed brightening, around orbital phase ~ 0.9 , could be consistent with this prediction.

6.3. Nature of the line-emitting region

As shown in Sect. 5, the geometry in the K -band emission lines is substantially different from what we see in the continuum. The best fit to the circumstellar environment in the He I and Br γ lines indicates a strongly-emitting Keplerian disc around the primary component. In this section, we present three possible interpretations for the physical origin of the line emission, either emission from the accretion region, an ionised gas accretion disc channeling circumstellar material to the star, or a decretion disc tracing material from the star being lost through stellar winds.

6.3.1. Accretion onto the primary

Brackett γ emission is a common marker of magnetospheric accretion in YSOs and is especially useful for accretion rate determination, since the luminosity of the line ($L_{\text{Br}\gamma}$) has been shown to be directly related to the accretion luminosity L_{acc} over a wide mass range from brown dwarfs to Herbig Ae stars (e.g. Muzerolle et al. 1998; Calvet et al. 2004). This relation follows a power law which is strongly dependent on stellar mass (Fairlamb et al. 2017).

For Herbig Ae objects, Donehew & Brittain (2011) derived the following relation:

$$\log(L_{\text{acc}}/L_{\odot}) = (0.9 \pm 0.2) \log(L_{\text{Br}\gamma}/L_{\odot}) + (3.3 \pm 0.7), \quad (5)$$

with similar values obtained by Mendigutía et al. (2011). From the above relation, the accretion rate \dot{M} can be derived:

$$L_{\text{acc}} = \frac{GM_* \dot{M}}{R_*}, \quad (6)$$

where M_* and R_* are respectively the mass and radius of the star. Using the Br γ luminosity for MWC 166 A calculated by Donehew & Brittain (2011) of $L_{\text{Br}\gamma} = (11 \pm 5) \times 10^{-3} L_{\odot}$, we can estimate the accretion luminosity and hence the mass accretion rate. This results in $L_{\text{acc}} \sim 35 \pm 65 L_{\odot}$ and subsequently

$\dot{M} \sim (3.9 \pm 7.4) \times 10^{-7} M_{\odot} \text{ yr}^{-1}$, which is in line with the typical mass accretion rate of $2 \times 10^{-7} M_{\odot} \text{ yr}^{-1}$ found by Mendigutía et al. (2011).

However, it must be noted that, with a mass of $12 M_{\odot}$, MWC 166 Aa is a Be star, leaving it outside of the regime where the $L_{\text{Br}\gamma} - L_{\text{acc}}$ relation has been calibrated. Indeed, Eq. 5 provides a systematic overestimate of L_{acc} for Be stars, according to Donehew & Brittain (2011). Furthermore, the large uncertainties inherent to the estimate of $L_{\text{Br}\gamma}$ by Donehew & Brittain (2011) result in very large errors on the propagated quantities. As a result, the above value for \dot{M} should be taken to be an order-of-magnitude estimate.

The strong Br γ signal is consistent with accretion, as is the youth of the system. However, the geometry of the line emission does not appear to be consistent with direct stellar accretion. The radius of the emission originates from a region further from the stellar surface than the $\sim 5R_{\star}$ which would be expected from accretion in Herbig Ae/Be stars (Bouvier et al. 2020). Furthermore, the geometry of the line emission is also stable over all epochs, with the red and blue lobes consistently located north-west and south-east of MWC 166 Aa, and with velocities consistent with Keplerian rotation, which is not expected of material being funnelled onto a stellar surface (Bouvier et al. 2007). As a result, the line emission does not appear to be tracing direct stellar accretion, but rather a process which is more spatially extended.

6.3.2. Inner gas accretion disc

The line emission might trace ionised gas in the inner region of the circumprimary gas disc. Based on hydrodynamic simulations, we expect that a stable circumprimary gas disc can exist out to one third of the binary separation (Artymowicz & Lubow 1994). This disc could accommodate the mass transport from the large-scale mass reservoir seen in far-infrared excess emission, over a circumbinary disc to the star. For MWC 166 A, the upper limit on the radius is $\sim 0.9 \text{ au}$ or $\sim 15 R_1$, which is in agreement with the observed location of the Br γ emission ($\sim 11.5 R_1$). These discs are often found around Herbig Ae/Be systems, which would be consistent with the age of the system (see Sect. 6.4). The emission would then be tracing ionised gas in Keplerian rotation around the star, rather than direct accretion onto the star. Kraus et al. (2012) found an example of such a disc around another young B-type close binary system, V921 Sco, using similar techniques. The Br γ line profiles were found to be similarly strong and narrow to those presented in this study for MWC 166 Aa. They also were similarly variable in intensity and wing strength, while still being consistent with a Keplerian disc.

However, the lack of evidence of direct accretion in our observations means that this scenario cannot be confirmed. Further observations at shorter wavelengths may show evidence of accretion, for example by showing emission closer to the stellar surface.

6.3.3. Be decretion disc

As a third scenario, we consider that the observed circumprimary emission might be associated with a decretion disc, as observed around classical Be stars. Classical Be stars are defined as non-supergiant B stars which have shown Balmer line emission at some point in time (Collins 1987). Generally very fast rotators, they typically host gaseous circumstellar discs characterised by a viscous decretion model (e.g. Lee et al. 1991; Carciofi 2011),

with material ejected by radiation pressure from the star forming a Keplerian disc. This disc is sustained by periodic outbursts from the star (Grundstrom et al. 2011), which leads to variability on a range of timescales from days to years (Labadie-Bartz et al. 2017).

Variability in the emission line profile is also common in decretion discs, with violet-to-red (V/R) variations meaning the red-shifted and blue-shifted wings of the line are commonly found at different relative strengths at different epochs (Rivinius et al. 2013) – Fig. 3 shows that such variations are indeed present in the spectrum of MWC 166 A, and the results in columns (3) and (4) of Table 7 quantify this. In the simplest of Keplerian models, the flux intensities of each wing should be equal. The observed deviation from this profile is due to the flux intensity of the disc being azimuthally asymmetrical (Porter & Rivinius 2003), which is most likely due to temperature or gas density enhancements in specific regions of the disc. Our observations, comprising only four epochs, are insufficient to characterise the observed variations in V/R ratio as being periodic or quasi-periodic, but previous studies (Hanuschik et al. 1995) indicate that, in general, these variations are cyclic in the long-term. Hummel & Hanuschik (1997) modelled a one-armed density wave precessing around the star as an explanation for these variations.

The rapidly changing V/R ratio is characteristic of Classical Be stars observed at intermediate inclinations (Catanzaro 2013). Such variations are generally not found in Herbig Be objects. Furthermore, the line-emitting region around the primary is rather extended, which is more consistent with decretion than accretion. We would assume Br γ emission from magnetospheric accretion to originate no more than $5R_{\star}$ from the star (Bouvier et al. 2020). However, we find that at all epochs, it is located well beyond the stellar surface. We estimated the radius of the emission by averaging the angular displacement in the blue and red wings of each line, with the results shown in column (5) of Table 7. These values do agree with each other in almost all circumstances, despite some slight variation between the two lines and epochs, with a general separation from the primary of $\sim 0.25 \text{ mas}$, or $\sim 11 R_1$. Comparing this value to other spectro-interferometric Be studies shows that it is consistent with that of a Classical Be disc, with the VLTI/AMBER survey by Cochetti et al. (2019) showing Br γ radii ranging between $3 - 13 R_{\star}$. The lack of dust in Be discs also correlates with our findings from the continuum fit, where we found no evidence for circumprimary dust.

In light of the above points, the decretion disc model cannot be excluded for the circumprimary emission. Previous photometric studies of MWC 166 A found evidence for periodic dissipation and regeneration of the circumstellar envelope around the primary star over a period of months (Pogodin et al. 2006), which is consistent with models and observations of Be stars and adds weight to this interpretation of the line emission.

This would be in contrast to previous characterisations of MWC 166 Aa as a Herbig Be star (Fairlamb et al. 2015), and is also supported by our isochrone interpolation: from Fig. 9, it can be seen that the large mass of the primary means that it is evolved beyond the protostellar stage at all age estimates. This is further supported by the relatively small near-infrared excess in the spectral energy distribution of MWC 166 A, suggesting that the circumstellar environment has been at least partially cleared of material. The observed far-infrared excess of the system at $\sim 100 \mu\text{m}$, however, is more supportive of the accretion disc scenario outlined in Sect. 6.3.2.

As a result, we can characterise the *K*-band line emission as originating in a Keplerian or quasi-Keplerian circumprimary gas

disc, as opposed to direct stellar accretion. Whether this is an accretion disc or a decretion disc is to be confirmed by future observations.

6.4. Constraining the age of the system

As Table 5 and Fig. 9 show, the primary star has already reached the main-sequence for all plausible age estimates, while the secondary is still in its pre-main-sequence stage at the youngest age estimates. By comparing the luminosities of the two stars at different ages to the flux ratios found from our interferometric observations, we can place some constraints on the age of the system.

We first performed the process described in Sect. 4.4 for every age isochrone in our CMD table between 100 kyr and 10 Myr. We then used the derived parameters to generate spectral energy distributions for both stars, using model atmospheres from Kurucz (1993). We then calculated values of f_2/f_1 at the central wavelengths of both the H - and K -bands, 1.65 μm and 2.2 μm respectively, to enable a comparison with the corresponding values from our continuum interferometry. The resulting flux ratios are plotted as the red lines on Fig. 11, with the H -band ratios in the upper panel and the K -band ratios in the lower panel.

The H -band flux ratio measurements show significant scatter between epochs, which might be due to scattered light contributions that are important towards shorter wavelengths. As described in Sect. 6.2, PIONIER will likely be more strongly affected by these contributions, while MIRC-X and the long CHARA baselines should be able to resolve out extended flux and separate the components more reliably. Therefore, we adopt the MIRC-X value of $f_2/f_1 = 0.484 \pm 0.014$ as our most reliable H -band flux ratio measurements, and mark this value with the blue line in the lower panel of Fig. 11.

The K -band continuum GRAVITY data shows much less variability, and therefore we chose to take the weighted average of the GRAVITY flux ratios is plotted on the lower panel of Fig. 11, corresponding to an average flux ratio of $f_2/f_1 = 0.399 \pm 0.021$.

Comparing the measured H and K -band flux ratio with the model values, we can exclude ages for the system of $\lesssim 500$ kyr. In the K -band, this is well beyond the 3σ significance level. For the H -band, this is only 2σ , but the range of ages < 500 kyr for which this is the case is very small, and only due to our relatively large mass uncertainties – which are themselves large because of the uncertainty on the system’s distance.

At such young ages, the near-infrared brightness of the secondary would exceed the primary, due to the low temperature of the secondary component, which is not supported by our interferometric observations. The upper age of the system is less well constrained, as the stars evolve very slowly once they reach the main-sequence (see Fig. 9). This can be seen in Fig. 11, where the models predict consistently $f_2/f_1 \sim 0.2$ for ages beyond 1 Myr. Our average continuum K -band flux ratio is larger than this, suggesting that the secondary component of the system is still in its pre-main-sequence stage. From our combined H and K -band constraints, we estimate the system age to $(7 \pm 2) \times 10^5$ yr. This young age is also consistent with the presence of circumstellar material (see Sect. 6.1). Such an age is also consistent with either the accretion or decretion disc models described in Sects. 6.3.2 and 6.3.3.

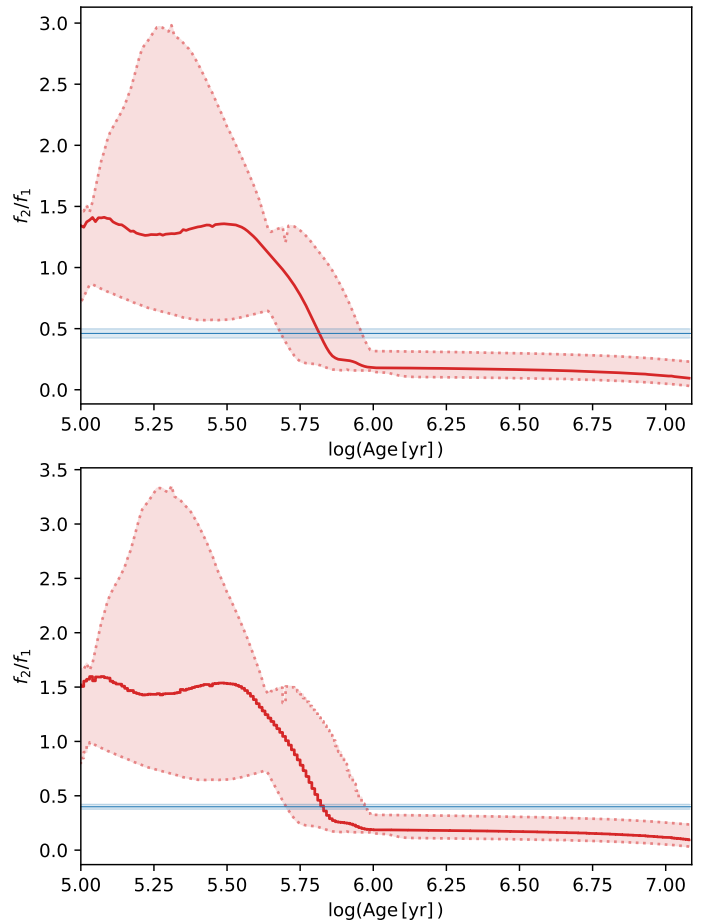


Fig. 11: Flux ratio f_2/f_1 plotted against $\log(\text{Age})$, for all isochrones (red lines), compared to interferometric flux ratios at the same wavelength (blue lines). The upper panel shows the flux ratio at 1.65 μm , while the lower panel shows the flux ratio at 2.2 μm – the central wavelengths for the H - and K -bands respectively. The lighter-shaded areas illustrate the uncertainty on each quantity.

7. Conclusions

In this study we have presented GRAVITY, PIONIER and MIRC-X observations of MWC 166 A that resolve the system in the near-infrared H -band and K -band with milliarcsecond resolution. We derived the astrometry of the system at 13 epochs and calculated a first fully three-dimensional orbital solution for the system. This orbit differs substantially from the RV-only orbits of Corporon & Lagrange (1999) and Pogodin et al. (2006), having a period twice as long. We subsequently constrained the dynamical system mass ($17.1 \pm 2.7 M_\odot$ for the photometric distance of 990 ± 50 pc found by Kaltcheva & Hilditch 2000) and the distance of the system, with our results excluding previous parallax measurements of the distance where $d < 500$ pc. Furthermore, we have calculated, for the first time, the individual masses of the primary and the secondary components of the system, which we found to be $M_1 = (12.19 \pm 2.18) M_\odot$ and $M_2 = (4.90 \pm 0.52) M_\odot$ respectively. We also found estimates for the other fundamental stellar parameters based on quadratic isochrone interpolation.

Furthermore, we see evidence for circumstellar emission, both in the dust continuum and in the He I and Br γ spectral lines, although they have different geometries. The geometry of the extended emission in the continuum is not well constrained, with

the best fit corresponding to an overresolved background halo. The variability of the continuum emission between epochs may be an indication of physical variability in the quantity of circumstellar dust, or might indicate that the geometry is more complex than assumed in our model. Characterising it in more detail will require additional interferometric observations, ideally at mid-infrared wavelengths.

On the other hand, the geometry of the He I and Br γ line emission is well constrained by our observations. Our models show emission in these lines to be localised around the primary, where the red-shifted and blue-shifted wings are spatially displaced, consistent with gas in a circumprimary disc. The large spatial extent of the line-emitting regions ($11.5 R_1$ for Br γ , $10.5 R_1$ for He I) and stable position angle orientation are inconsistent with an origin in magnetospheric accretion or boundary-layer accretion, but support the hypothesis that the line emission is tracing an ionised gas disc. This gas disc might either be fed by mass infall from outside the binary, or represent a decretion disc forming through mass-loss from the primary.

Finally, we constrain the age of the system to $(7 \pm 2) \times 10^5$ yr, based on the measured flux ratio of the components. We find that the primary is a main-sequence Be star, while the secondary is a Herbig Be object still in the process of gravitational contraction onto the main sequence.

Acknowledgements. We acknowledge support from an STFC studentship (No. 109106G), an STFC Consolidated Grant (ST/V000721/1), and European Research Council Starting Grant "ImagePlanetFormDiscs" (Grant Agreement No. 639889) and Consolidated Grant "GAIA-BIFROST" (Grant Agreement No. 101003096). Travel support was provided by STFC PATT grant ST/S005293/1. MIRC-X received funding from the European Research Council (ERC) under the European Union's Horizon 2020 research and innovation programme (Grant No. 639889). JDM acknowledges funding for the development of MIRC-X (NASA-XRP NNX16AD43G, NSF-AST 1909165) and MYSTIC (NSF-ATI 1506540, NSF-AST 1909165). This research has made use of the VizieR catalogue access tool, CDS, Strasbourg, France. The original description of the VizieR service was published in Ochsenbein et al. (2000). This research has made use of the Jean-Marie Mariotti Center JSDC catalogue⁸. This research has made use of the Jean-Marie Mariotti Center OidB service available at <http://oidb.jmmc.fr>. Analysis in this work was based on observations collected at the European Organisation for Astronomical Research in the Southern Hemisphere under ESO programme(s) 098.C-0910(A) (GRAVITY); 190.C-0963(A), 190.C-0963(B), 102.C-0701(B), 104.C-0737(A), 104.C-0737(B), 104.C-0737(C), 106.21JU.001, 106.21JU.002, 106.21JU.003 (PIONIER). This research has made use of the PIONIER data reduction package of the Jean-Marie Mariotti Center⁹. This work has made use of data from the European Space Agency (ESA) mission *Gaia* (<https://www.cosmos.esa.int/gaia>), processed by the *Gaia* Data Processing and Analysis Consortium (DPAC, <https://www.cosmos.esa.int/web/gaia/dpac/consortium>). Funding for the DPAC has been provided by national institutions, in particular the institutions participating in the *Gaia* Multilateral Agreement. We thank the referee for their insightful comments

References

Anthoz, F., Ménard, F., Pinte, C., et al. 2015, *A&A*, 574, A41
 Anugu, N., Le Bouquin, J.-B., Monnier, J. D., et al. 2020, *AJ*, 160, 158
 Artymowicz, P. & Lubow, S. H. 1994, *ApJ*, 421, 651
 Bailer-Jones, C. A. L., Rybizki, J., Fousneau, M., Demleitner, M., & Andrae, R. 2021, *AJ*, 161, 147
 Bailer-Jones, C. A. L., Rybizki, J., Fousneau, M., Mantelet, G., & Andrae, R. 2018, *AJ*, 156, 58
 Baraffe, I., Homeier, D., Allard, F., & Chabrier, G. 2015, *A&A*, 577, A42
 Boffin, H. M. J. 2012, in *Orbital Couples: Pas de Deux in the Solar System and the Milky Way*, ed. F. Arenou & D. Hestroffer, 41–44
 Bourges, L., Mella, G., Lafrasse, S., et al. 2017, *VizieR Online Data Catalog*, 2346
 Bouvier, J., Alencar, S. H. P., Harries, T. J., Johns-Krull, C. M., & Romanova, M. M. 2007, in *Protostars and Planets V*, ed. B. Reipurth, D. Jewitt, & K. Keil, 479

⁸ Available at: http://www.jmmc.fr/catalogue_jsdc.htm

⁹ Available at <http://www.jmmc.fr/pionier>

Bouvier, J., Perraut, K., Le Bouquin, J. B., et al. 2020, *A&A*, 636, A108
 Bressan, A., Marigo, P., Girardi, L., et al. 2012, *Monthly Notices of the Royal Astronomical Society*, 427, 127, aDS Bibcode: 2012MNRAS.427..127B
 Calvet, N., Muzerolle, J., Briceño, C., et al. 2004, *AJ*, 128, 1294
 Carciofi, A. C. 2011, in *Active OB Stars: Structure, Evolution, Mass Loss, and Critical Limits*, ed. C. Neiner, G. Wade, G. Meynet, & G. Peters, Vol. 272, 325–336
 Catanzaro, G. 2013, *A&A*, 550, A79
 Chen, C., Franchini, A., Lubow, S. H., & Martin, R. G. 2019, *MNRAS*, 490, 5634
 Chen, Y., Bressan, A., Girardi, L., et al. 2015, *Monthly Notices of the Royal Astronomical Society*, 452, 1068, aDS Bibcode: 2015MNRAS.452.1068C
 Chen, Y., Girardi, L., Bressan, A., et al. 2014, *Monthly Notices of the Royal Astronomical Society*, 444, 2525, aDS Bibcode: 2014MNRAS.444.2525C
 Choi, J., Dotter, A., Conroy, C., et al. 2016, *ApJ*, 823, 102
 Cieza, L. A., Padgett, D. L., Allen, L. E., et al. 2009, *ApJ*, 696, L84
 Clariá, J. J. 1974, *AJ*, 79, 1022
 Cochetti, Y. R., Arcos, C., Kanaan, S., et al. 2019, *A&A*, 621, A123
 Collins, George W., I. 1987, in *IAU Colloq. 92: Physics of Be Stars*, ed. A. Slettebak & T. P. Snow, 3
 Cororon, P. & Lagrange, A.-M. 1999, *A&AS*, 136, 429
 Curé, M., Rial, D. F., Cassetti, J., Christen, A., & Boffin, H. M. J. 2015, *A&A*, 573, A86
 Donehew, B. & Brittain, S. 2011, *AJ*, 141, 46
 Doyle, L. R., Carter, J. A., Fabrycky, D. C., et al. 2011, *Science*, 333, 1602
 Dunhill, A. C., Cuadra, J., & Dougados, C. 2015, *MNRAS*, 448, 3545
 ESA, ed. 1997, *ESA Special Publication*, Vol. 1200, *The HIPPARCOS and TYCHO catalogues. Astrometric and photometric star catalogues derived from the ESA HIPPARCOS Space Astrometry Mission*
 Fabricius, C., Høg, E., Makarov, V. V., et al. 2002, *A&A*, 384, 180
 Fairlamb, J. R., Oudmaijer, R. D., Mendigutia, I., Ilee, J. D., & van den Ancker, M. E. 2015, *MNRAS*, 453, 976
 Fairlamb, J. R., Oudmaijer, R. D., Mendigutia, I., Ilee, J. D., & van den Ancker, M. E. 2017, *MNRAS*, 464, 4721
 Finkenzeller, U. & Mundt, R. 1984, *A&AS*, 55, 109
 Foreman-Mackey, D. 2016, *The Journal of Open Source Software*, 1, 24
 Freudling, W., Romaniello, M., Bramich, D. M., et al. 2013, *A&A*, 559, A96
 Frost, A. J., Bodensteiner, J., Rivinius, T., et al. 2022, *A&A*, 659, L3
 Gallenne, A., Pietrzyński, G., Graczyk, D., et al. 2018, *A&A*, 616, A68
 Gravity Collaboration, Abuter, R., Accardo, M., et al. 2017, *A&A*, 602, A94
 Grundstrom, E. D., McSwain, M. V., Aragona, C., et al. 2011, *Bulletin de la Societe Royale des Sciences de Liege*, 80, 371
 Hanuschik, R. W., Hummel, W., Dietle, O., & Sutorius, E. 1995, *A&A*, 300, 163
 Herbst, W. & Assousa, G. E. 1977, *ApJ*, 217, 473
 Hummel, W. & Hanuschik, R. W. 1997, *A&A*, 320, 852
 Kaltcheva, N. T. & Hilditch, R. W. 2000, *MNRAS*, 312, 753
 Kluska, J., Benisty, M., Soulez, F., et al. 2016, *A&A*, 591, A82
 Kraus, S., Calvet, N., Hartmann, L., et al. 2012, *ApJ*, 752, 11
 Kraus, S., Kreplin, A., Young, A. K., et al. 2020, *Science*, 369, 1233
 Kraus, S., Monnier, J. D., Anugu, N., et al. 2018, in *Society of Photo-Optical Instrumentation Engineers (SPIE) Conference Series*, Vol. 10701, *Optical and Infrared Interferometry and Imaging VI*, ed. M. J. Creech-Eakman, P. G. Tuthill, & A. Mérand, 1070123
 Kraus, S., Weigelt, G., Balega, Y. Y., et al. 2009, *A&A*, 497, 195
 Kreplin, A., Tambovtseva, L., Grinin, V., et al. 2018, *MNRAS*, 476, 4520
 Kurucz, R. L. 1993, *VizieR Online Data Catalog*, VI/39
 Labadie-Bartz, J., Pepper, J., McSwain, M. V., et al. 2017, *AJ*, 153, 252
 Lazareff, B., Berger, J. P., Kluska, J., et al. 2017, *A&A*, 599, A85
 Le Bouquin, J. B., Berger, J. P., Lazareff, B., et al. 2011, *A&A*, 535, A67
 Lee, U., Osaki, Y., & Saio, H. 1991, *MNRAS*, 250, 432
 Li, M. & Xiao, L. 2016, *ApJ*, 820, 36
 Marigo, P., Girardi, L., Bressan, A., et al. 2017, *ApJ*, 835, 77
 Massey, P., Morrell, N. I., Neugent, K. F., et al. 2012, *ApJ*, 748, 96
 Mathieu, R. D. 1994, *ARA&A*, 32, 465
 Mendigutia, I., Calvet, N., Montesinos, B., et al. 2011, *A&A*, 535, A99
 Monnier, J. D. & Millan-Gabet, R. 2002, *ApJ*, 579, 694
 Muzerolle, J., Flaherty, K., Balog, Z., Beck, T., & Gutermuth, R. 2019, *ApJ*, 877, 29
 Muzerolle, J., Hartmann, L., & Calvet, N. 1998, *AJ*, 116, 455
 Nagel, E., D'Alessio, P., Calvet, N., et al. 2010, *ApJ*, 708, 38
 Ochsenbein, F., Bauer, P., & Marcout, J. 2000, *A&AS*, 143, 23
 Pastorelli, G., Marigo, P., Girardi, L., et al. 2019, *Monthly Notices of the Royal Astronomical Society*, 485, 5666, aDS Bibcode: 2019MNRAS.485.5666P
 Pichardo, B., Sparke, L. S., & Aguilar, L. A. 2005, *MNRAS*, 359, 521
 Pogodin, M. A., Malanushenko, V. P., Kozlova, O. V., Tarasova, T. N., & Franco, G. A. P. 2006, *A&A*, 452, 551
 Porter, J. M. & Rivinius, T. 2003, *PASP*, 115, 1153
 Rivinius, T., Carciofi, A. C., & Martayan, C. 2013, *A&A Rev.*, 21, 69
 Shevchenko, V. S., Ezhkova, O. V., Ibrahimov, M. A., van den Ancker, M. E., & Tjin A Dje, H. R. E. 1999, *MNRAS*, 310, 210
 Siess, L., Dufour, E., & Forestini, M. 2000, *A&A*, 358, 593
 Stassun, K. G., Feiden, G. A., & Torres, G. 2014, *New A Rev.*, 60, 1
 Tang, J., Bressan, A., Rosenfield, P., et al. 2014, *Monthly Notices of the Royal Astronomical Society*, 445, 4287, aDS Bibcode: 2014MNRAS.445.4287T
 ten Brummelaar, T. A., McAlister, H. A., Ridgway, S. T., et al. 2005, *ApJ*, 628, 453
 Tjin A Dje, H. R. E., van den Ancker, M. E., Blondel, P. F. C., et al. 2001, *MNRAS*, 325, 1441
 Tokovinin, A. 1992, in *Astronomical Society of the Pacific Conference Series*, Vol. 32, *IAU Colloq. 135: Complementary Approaches to Double and Multiple Star Research*, ed. H. A. McAlister & W. I. Hartkopf, 573

Appendix A: PMOIREd line models

Below we show the full set of He I and Br γ line models for the four GRAVITY epochs, discussed in Sects. 3.2 and 5. The figures comprise nine panels, laid out equivalently to those in Fig. 10.

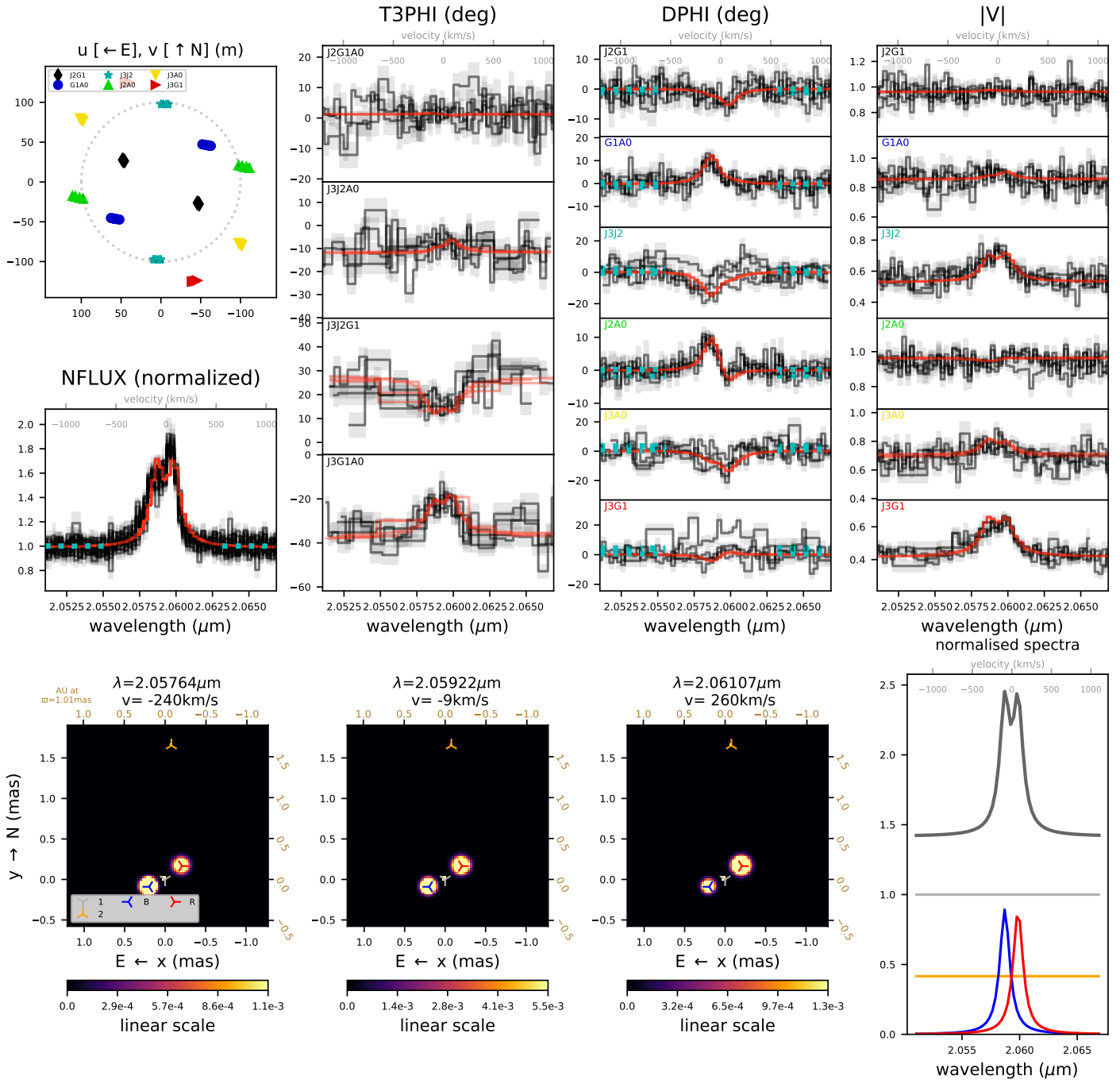


Fig. A.1: 2017-03-14, He I

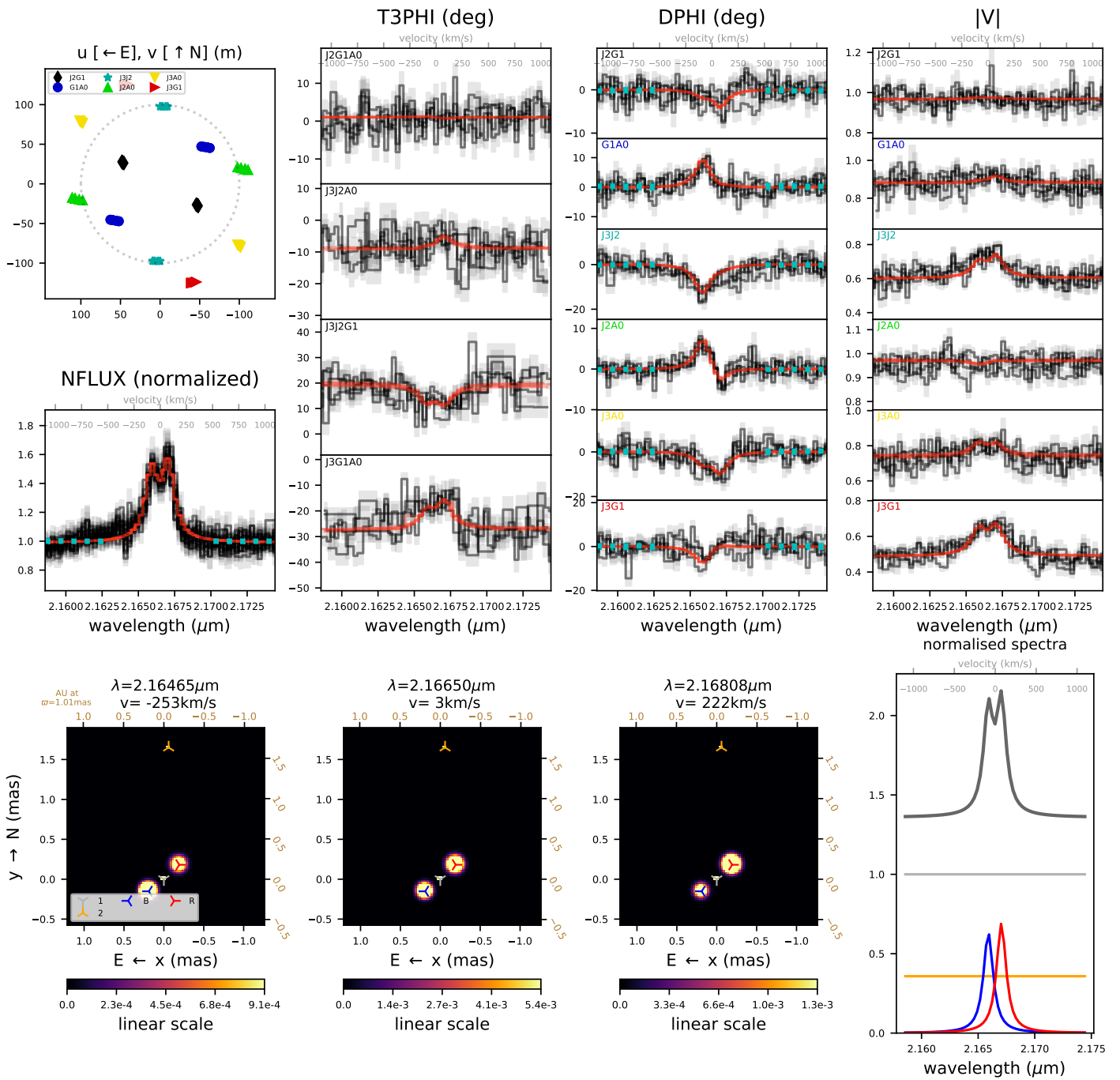


Fig. A.2: 2017-03-14, Br γ

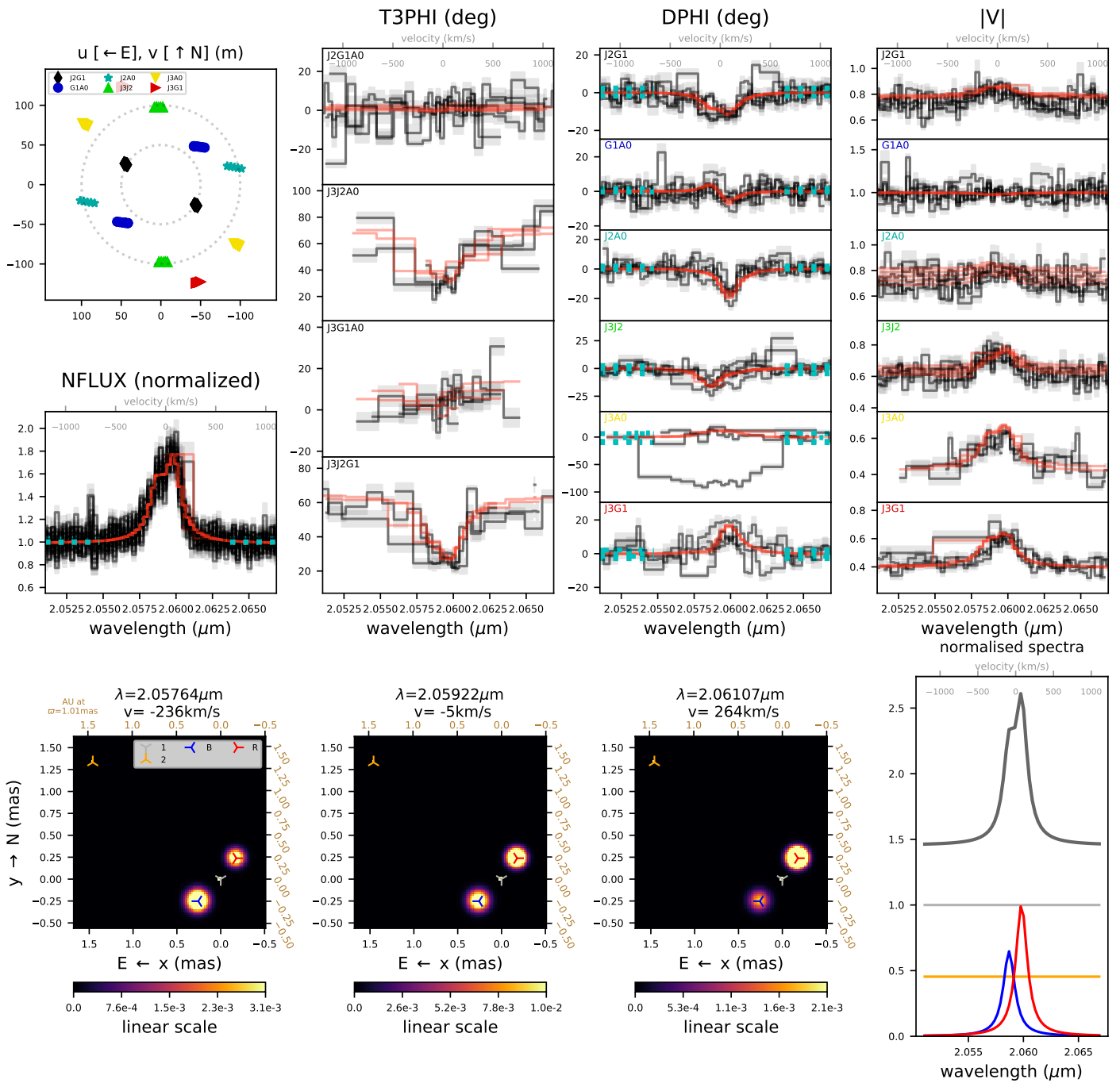


Fig. A.3: 2017-04-27, He I

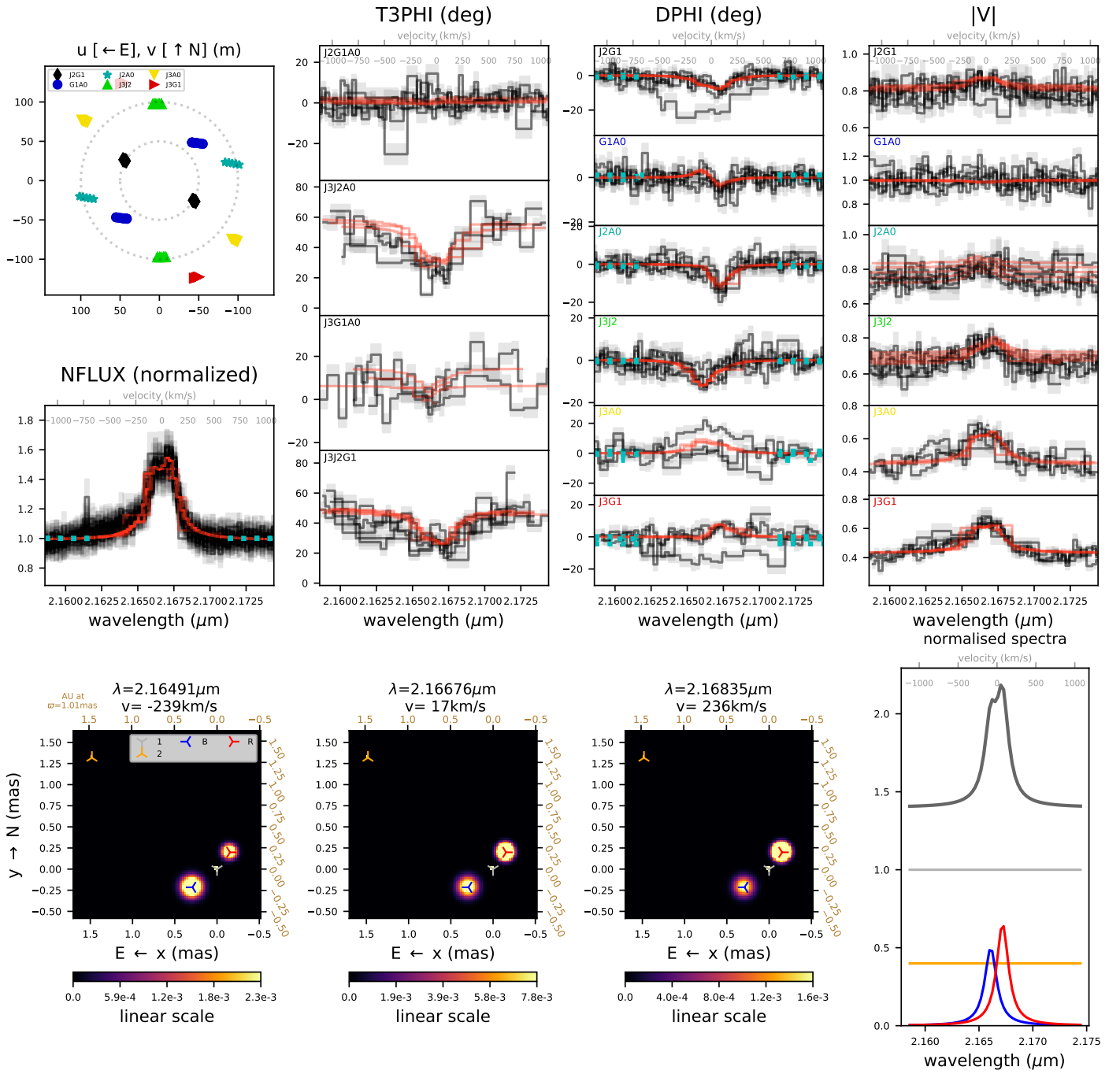


Fig. A.4: 2017-04-27, Br γ

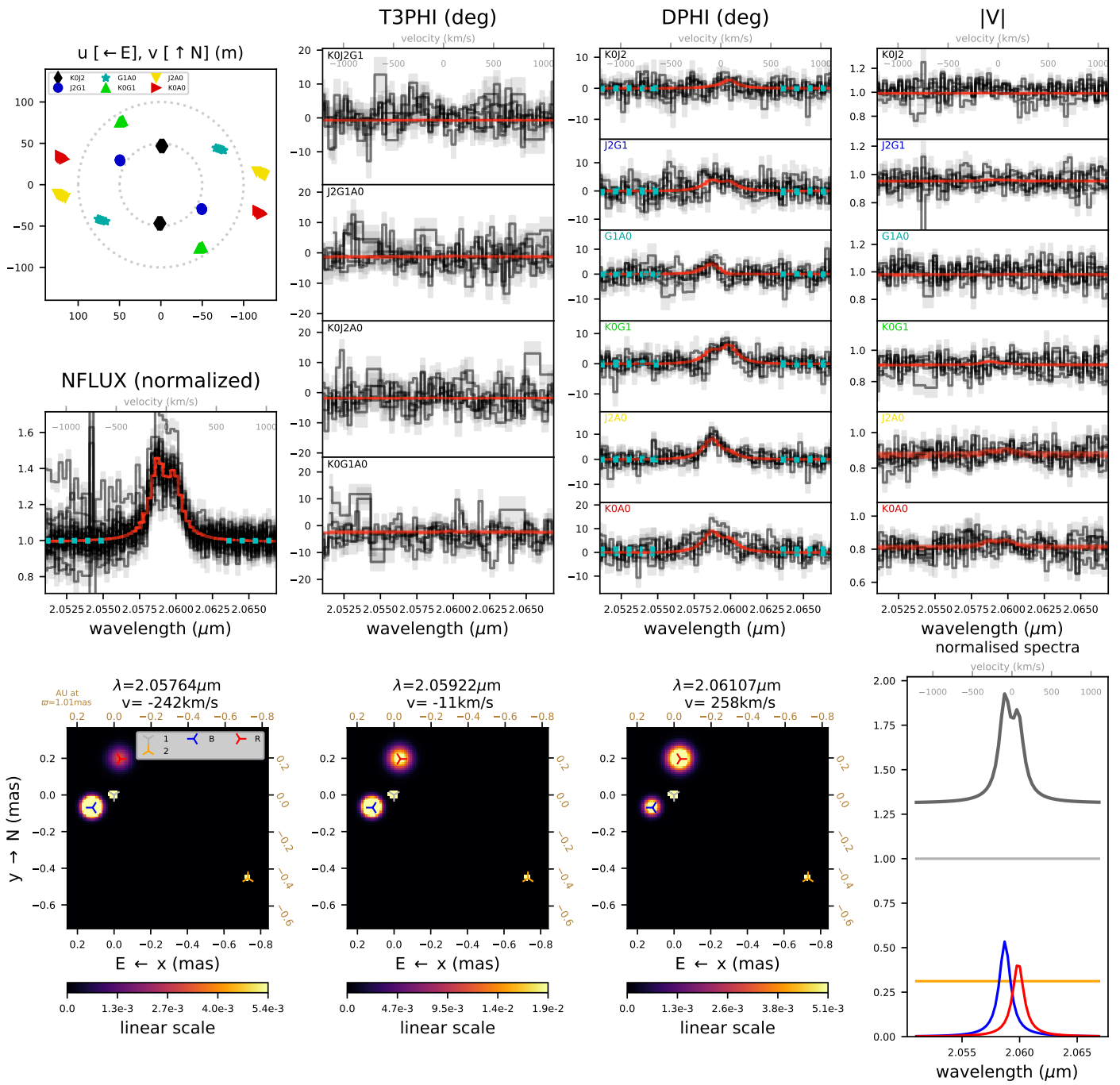


Fig. A.5: 2018-01-11, He I

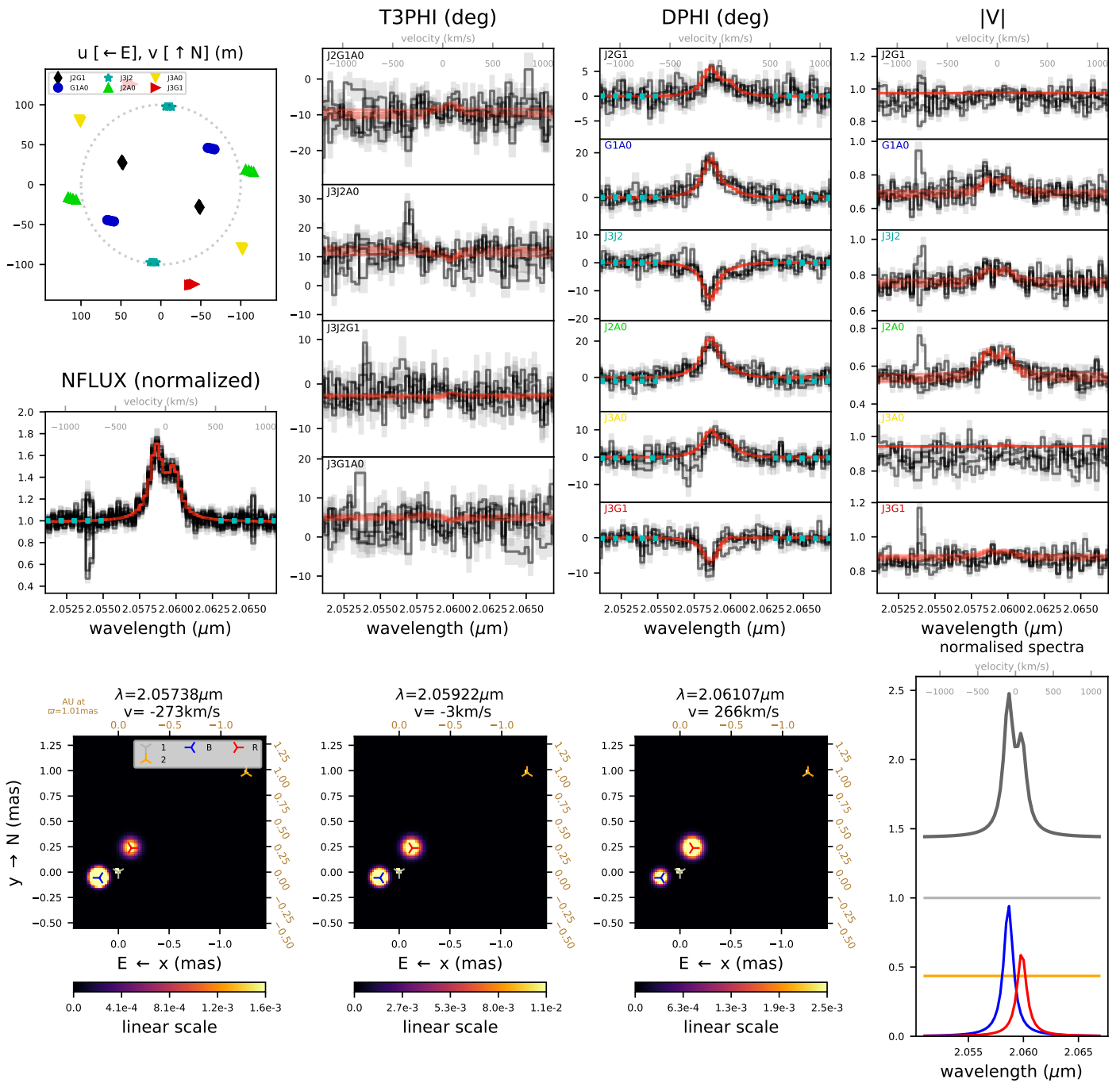


Fig. A.7: 2018-02-06, He I

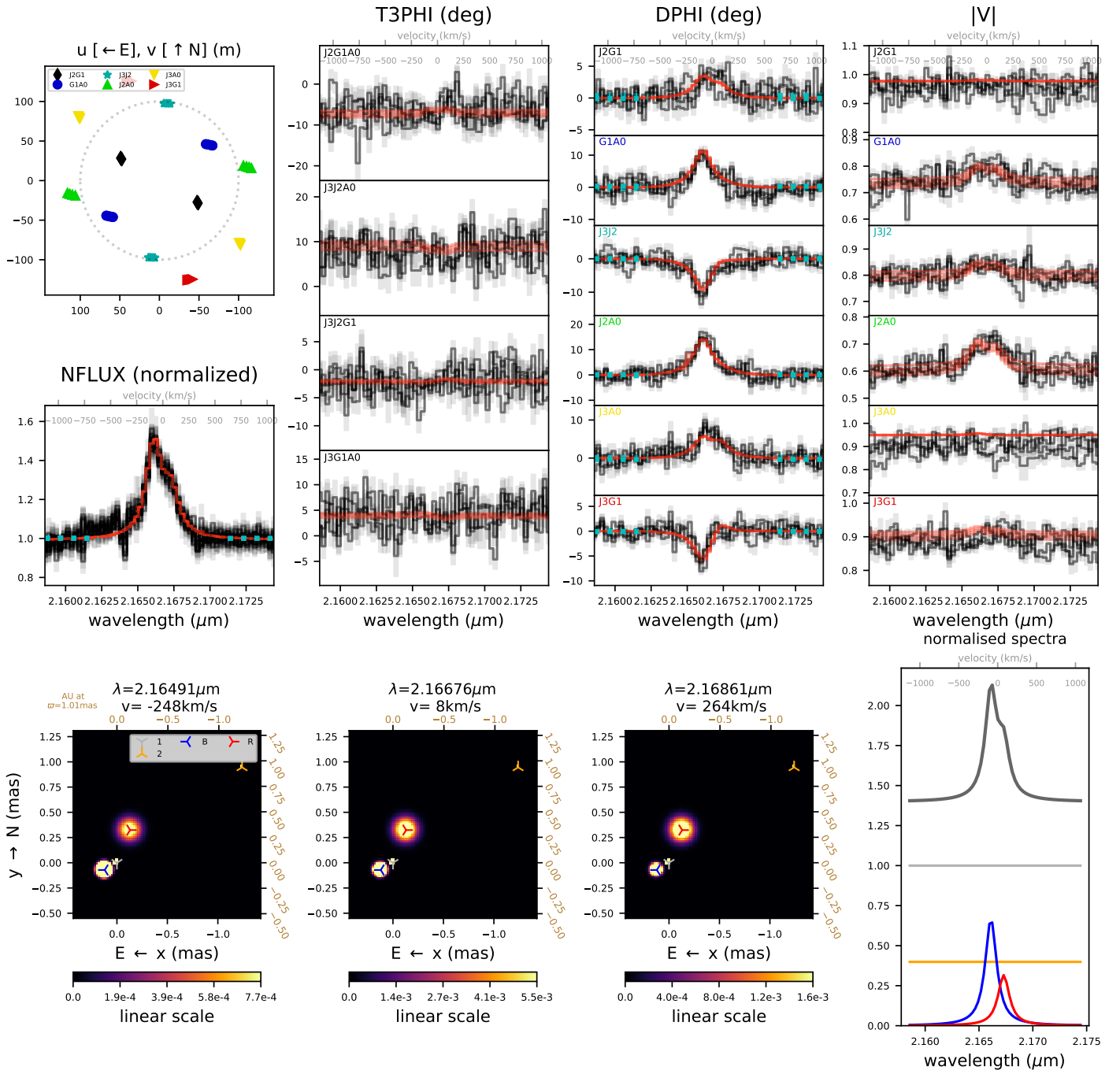


Fig. A.8: 2018-02-06, Br γ